AD-A032 697 INTERNATIONAL BUSINESS MACHINES CORP HOPEWELL JUNCTIO--ETC F/G 20/2
DEFECT STRUCTURE IN GAAS.(U)
SEP 76 G H SCHWUTTKE F19628-75-C-0174
UNCLASSIFIED IBM-TR-22.2065 RADC-TR-76-256 NL

1 OF 2
ADA032697

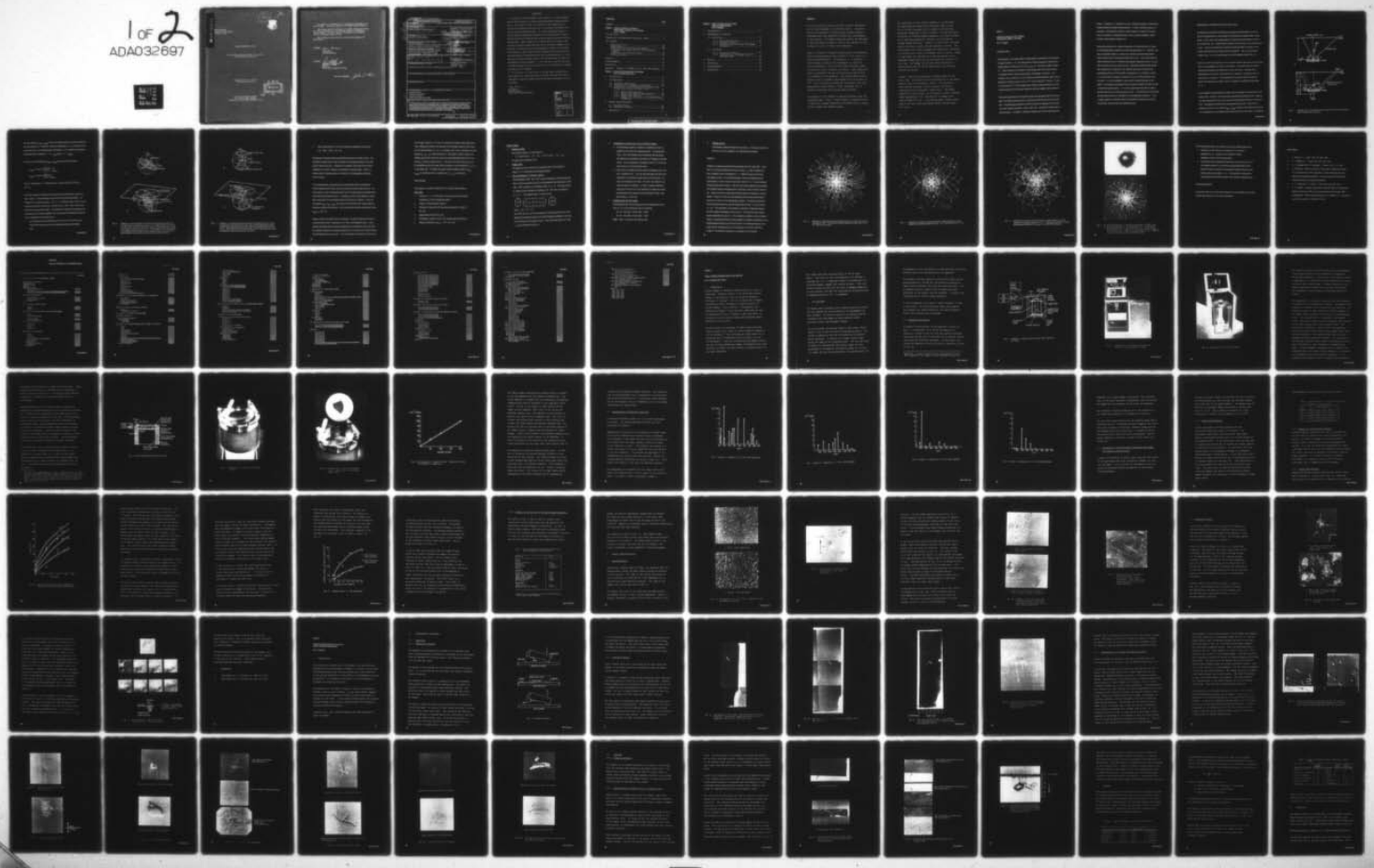

RADC-TR-76-256
Final Technical Report
September 1976

DEFECT STRUCTURE IN GaAs

International Business Machines Corporation
System Products Division

ROME AIR DEVELOPMENT CENTER
AIR FORCE SYSTEMS COMMAND
GRIFFISS AIR FORCE BASE, NEW YORK 13441

Dr. Guenter H. Schwuttke is the responsible investigator for this contract. Jane Bruce (ETSO), is the RADC Contract Monitor.

This report has been reviewed by the RADC Information Office (OI) and is releasable to the National Technical Information Service (NTIS). At NTIS it will be releasable to the General public, including foreign nations.

This technical report has been reviewed and approved for publication.

APPROVED: Jane Bruce

JANE BRUCE
Contract Monitor

APPROVED: Robert M. Barrett

ROBERT M. BARRETT
Director
Solid State Sciences Division

FOR THE COMMANDER: John P. Huss

Unclassified
SECURITY CLASSIFICATION OF THIS PAGE (When Data Entered)

REPORT DOCUMENTATION PAGE

READ INSTRUCTIONS BEFORE COMPLETING FORM

1. REPORT NUMBER: RADC-TR-76-256	2. GOVT ACCESSION NO.
3. RECIPIENT'S CATALOG NUMBER	
4. TITLE (and Subtitle): DEFECT STRUCTURE IN GaAs •	5. TYPE OF REPORT & PERIOD COVERED: Scientific - Final for Period 1 June 1975 - 31 May 1976
6. PERFORMING ORG. REPORT NUMBER: IBM-TR-22.2065	
7. AUTHOR(s): Guenter H. Schwuttke	8. CONTRACT OR GRANT NUMBER(s): F19628-75-C-0174
9. PERFORMING ORGANIZATION NAME AND ADDRESS: IBM Corporation, System Products Division, East Fishkill Labs, Hopewell Junction, New York 12533	10. PROGRAM ELEMENT, PROJECT, TASK AREA & WORK UNIT NUMBERS: 5620-03-08, 61102F
11. CONTROLLING OFFICE NAME AND ADDRESS: Deputy for Electronic Technology (RADC), Hanscomb AFB, Massachusetts 01731, Contract Monitor: Jane Bruce / ETSO	12. REPORT DATE: September 1976
	13. NUMBER OF PAGES: 96
14. MONITORING AGENCY NAME & ADDRESS (if different from Controlling Office): Final rept. 1 Jun 75 - 31 May 76,	15. SECURITY CLASS. (of this report): Unclassified
	15a. DECLASSIFICATION/DOWNGRADING SCHEDULE

16. DISTRIBUTION STATEMENT (of this Report)

Approved for public release; distribution unlimited.

12 96 pp.

17. DISTRIBUTION STATEMENT (of the abstract entered in Block 20, if different from Report)

18. SUPPLEMENTARY NOTES

19. KEY WORDS (Continue on reverse side if necessary and identify by block number)

Kossel Patterns
Computer Generation
Gallium Arsenide
Impact Sound Stressing (ISS)

20. ABSTRACT (Continue on reverse side if necessary and identify by block number)

A unified computer program is presented, which is useful for the generation of indexed Kossel, pseudo-Kossel, Kikuchi, and channeling maps. The application of Impact Sound Stressing, a novel technique to introduce damage into wafer surfaces, is discussed for GaAs. Equipment and operational parameters are given. Impact Sound Stress induced damage in GaAs surfaces is characterized by light optical and scanning electron microscopy.

DD FORM 1 JAN 73 1473 EDITION OF 1 NOV 65 IS OBSOLETE

Unclassified 401 914
SECURITY CLASSIFICATION OF THIS PAGE (When Data Entered)

EVALUATION

1. This report is the Final Report on the contract. It covers research done on characterization of gallium arsenide materials during the period June 1, 1975 to May 31, 1976. The objective of this research was to evaluate the crystalline perfection and to characterize the defect structure of gallium arsenide materials. For crystal perfection studies, a unified computer program was developed for the interpretation of Kossel, Kikuchi and electron channeling maps obtained during x-ray and/or electron beam analysis. These programs will be applied directly in house to the analysis of gallium arsenide materials and can be easily extended to new materials of interest such as indium phosphide and other III-V materials. The technique of Impact Sound Stressing, developed by the contractor has many applications to GaAs material and device characterization. It can be applied to evaluate polishing effects, fracture properties and effects of microdamage on device properties. It also provides a means for the study of damage propagation and for investigation of the possibilities of damage gettering in III-V compounds.

2. The above work is of value since it provides basic knowledge which makes possible the characterization of the defect structure and thus the improvement of gallium arsenide materials and device structures for use in AF systems.

Jane Bruce

JANE BRUCE
Contract Monitor
Solid State Sciences Division

CONTENTS

Chapter 3. Depth of Damage Induced in GaAs by Impact Sound Stressing (ISS) by R. G. Dessauer

SUMMARY

The Kossel pattern technique provides valuable information on the crystallography of crystalline solids. Interpretation of such patterns is difficult and recently computer techniques have been employed to obtain maps corresponding to the patterns. Published techniques require the knowledge of one experimental parameter, such as the specimen to film distance, in order to employ such techniques.

Chapter 1 presents a computer program capable of generating Kossel and pseudo-Kossel maps "directly" of the type as is observed experimentally. Consequently, it is possible to study changes in Kossel line arrangements as caused by varying parameters, such as Kossel camera constant, sample orientation, lattice constant, and others. Such changes are simply "programmed" and the resulting Kossel maps display the influence of the parameter. The program makes possible absolute lattice parameter measurements with an accuracy of 10^{-4}. This is achieved through the recording of just "one" experimental Kossel pattern. Other techniques rely on multiple recordings with varying camera constant.

The program is also capable of generating Kikuchi maps and channeling maps. Thus, a single program is presented which is useful for computer generation of indexed Kossel, pseudo-Kossel, Kikuchi and channeling maps.

The second part of this report (Chapters 2, 3) describes the application of Impact Sound Stressing (ISS) to GaAs. ISS is a novel technique that is capable of introducing mechanical damage into crystal surfaces. ISS was previously successful in studying damage propagation in silicon surfaces and in improving generation lifetime in silicon wafers through damage gettering. Chapter 2 of this report describes specialized impact sound stressing equipment for GaAs. The determination of various equipment and operational parameters is discussed and a table of parameter values is given. Graphs of input power and time period of ISS application versus obtainable damage densities are developed from a matrix of test runs. ISS damage at the GaAs surface and below is characterized with the aid of light optical and scanning electron microscopy.

Chapter 3 describes measurements of damage depth in GaAs due to ISS. Two methods for the determination of ISS damage depth in GaAs are described in detail. The techniques, bevelling and cleaving, involve structure etching and scanning electron microscopy, respectively. ISS damage induced at 10 watts power, for 60 seconds, reaches a maximum depth approaching 30 μm. The majority of damage sites reach a depth of 10 μm. A decreasing number reaches deeper than 10 μm, and a small percentage reaches maximum depth of $\approx$ 30 μm.

Chapter 1

COMPUTER GENERATION OF KOSSEL AND PSEUDO-KOSSEL LINE MAPS

by H. F. Kappert

INTRODUCTION

The divergent x-ray beam method is often used for quantitative strain analysis of single crystals (1, 2), for measurement of lattice parameters originated by compositional variation such as in $GaAs_{1-x}P_x$ (3), and also for defect studies (4). Kossel cameras are available to take photographs of so-called "Kossel" or "pseudo-Kossel" patterns generated by a divergent x-ray beam. The method is not as sensitive as x-ray double crystal diffractometry where lattice parameter variations of up to $\Delta d/d = 10^{-8}$ can be measured. However, if $\Delta d/d$ is of the order of 10^{-4} the divergent beam method is experimentally more convenient because of much shorter exposure times and simpler instrumentation.

Difficulties encountered in evaluating Kossel line data generated by the divergent x-ray beam technique arise in indexing the Kossel lines forming the pattern. The indexing procedure is relatively simple for samples with a known low order surface orientation, such as (001) etc., and also for Kossel lines of high symmetry. In general, indexing of Kossel lines is time-consuming and

tedious. Therefore, it is desirable to have a computer program for generating indexed Kossel and pseudo-Kossel patterns. If such a computer program is available, it also becomes possible to study changes in Kossel line arrangements as caused by varying parameters such as sample orientation, lattice constant, Kossel camera constant, etc.

Published procedures for computer generation of Kossel patterns are based on the stereographic projection for Kossel line generation (5). However, this type of projection results in circles only whereas true Kossel and pseudo-Kossel patterns show ellipses and hyperbolas as well. Thus these programs require additional work in transforming computer generated patterns into the type of patterns observed experimentally. Experience gained during writing and working with a program for the computer generation of Kikuchi and channeling pattern for TEM and SEM investigations (6) indicated to us that it is not desirable to program a computer to carry out this additional transformation. It is more expedient to use the new concept described in this report. This program generates Kossel and pseudo-Kossel line maps directly as observed experimentally. It is a short program and can also be used to generate Kikuchi and channeling maps as well -- if the last step of calculating the data before plotting is replaced by the stereographic projection. Thus, a single program is presented capable of generating Kossel lines, pseudo-Kossel lines, Kikuchi maps and channeling maps.

GEOMETRICAL CONSIDERATIONS AND BASIC IDEAS

By definition true Kossel line patterns are produced by diffraction of a source point of characteristics x-rays located in the surface of the sample under investigation. Such x-rays can be generated by an electron beam focussed on the sample surface (Fig. 1a). Pseudo-Kossel patterns are produced by non-characteristic x-rays. They are generated by focussing the electron beam on a small area of material different than the sample under investigation. The x-ray producing material (e.g., Cu) is at some distance b from the sample surface (Fig. 1b).

Figures 1a,b show the geometry of the two types of pattern generation assuming that the x-ray wavelength is the same in both cases. In the case of the true Kossel pattern the envelope of the diffracted x-rays is true cone. The cone axis is perpendicular to the set of (hkℓ) planes but, in general, is inclined to the surface normal at an angle β. The intersection of the Kossel cone with the film plane (the Kossel line) is either a circle, an ellipse or a hyberbola depending on β.

For the pseudo-Kossel pattern the Kossel cone is distorted for the same set of net planes (hkℓ). However, the cone can be reconstructed using the mirror image of the source produced by the x-rays in good Bragg reflection along the sample surface. The difference between the reconstructed cone in Fig. 1b and the true Kossel cone in Fig. 1a is a shift (x_{shift}, y_{shift}) relative to the electron beam axis. As a consequence the intersecting line of the cone with the film plane is shifted by

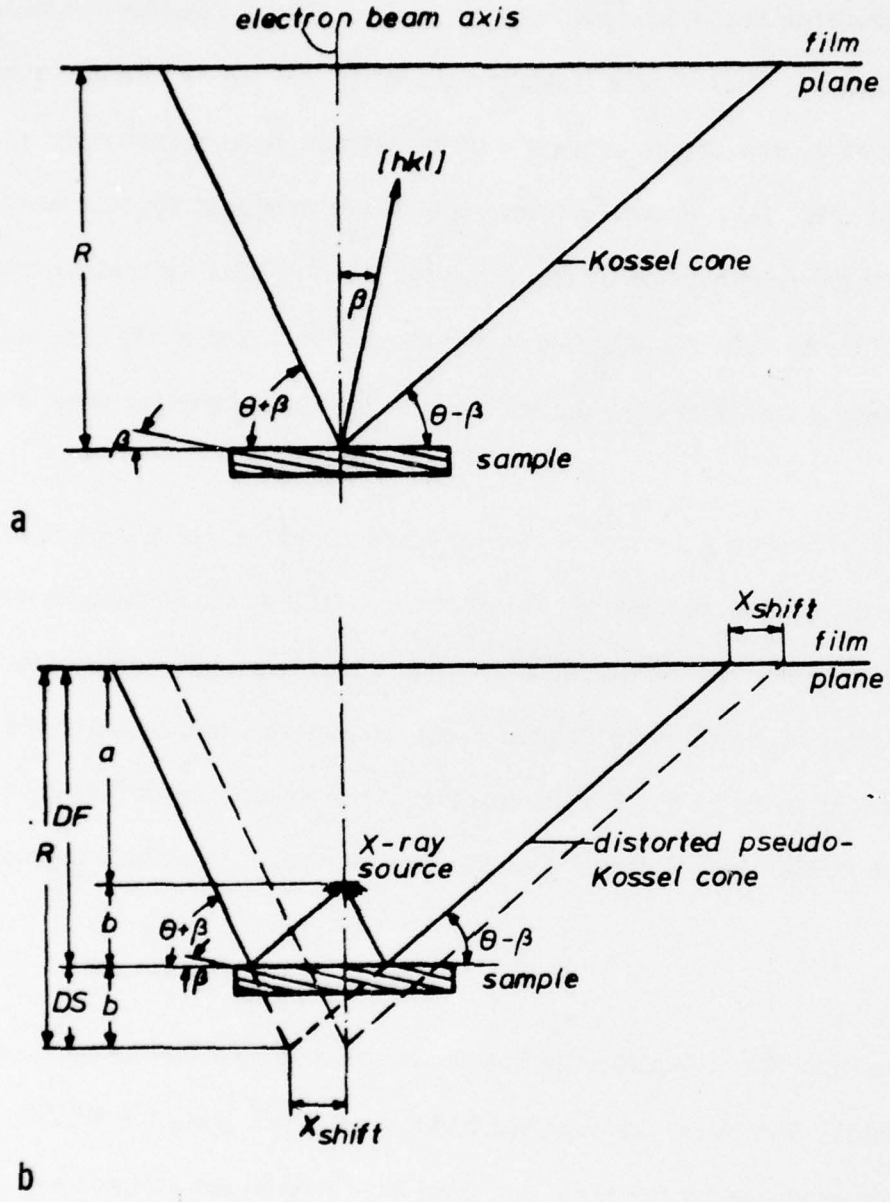

Fig. 1. Geometry of x-ray reflection in the case of a) a true Kossel pattern and b) pseudo-Kossel pattern.

the same amount (x_{shift}, y_{shift}) toward the electron beam axis with reference to the true Kossel line. Therefore, using the coordinates (x', y') of points on the true Kossel line, the corresponding coordinates (x, y) of points on the pseudo-Kossel line can be deduced: $x = x' + x_{shift}$ and $y = y' + y_{shift}$.

From Fig. 1b the coordinates x_{shift}, y_{shift} can be derived as follows:

$$x_{shift} = 2b \tan \beta_x \frac{\tan^2 \theta + 1}{\tan^2 \theta - \tan \beta_x}$$

$$y_{shift} = 2b \tan \beta_y \frac{\tan^2 \theta + 1}{\tan^2 \theta - \tan \beta_y}$$

with θ = Bragg angle, b = distance source - sample and $\tan^2 \beta = \tan^2 \beta_x + \tan^2 \beta_y$.

The basic concept of generating Kossel and pseudo-Kossel lines is shown in Figs. 2 and 3. These drawings are made for the true Kossel situation. We consider two orthonormal bases: the ($\hat{x}$, $\hat{y}$, $\hat{z}$) standard basis, with the z-axis parallel to the electron beam axis, and the [(100), (010), (001)] cubic basis fixed with the crystalline sample. Calculating each Kossel line separately the cubic basis will be rotated together with the crystal by coordinate transformations in reference to the standard base:

1. into a position where calculating the coordinates of the intersecting lines of the Kossel cone with the projection sphere is convenient and

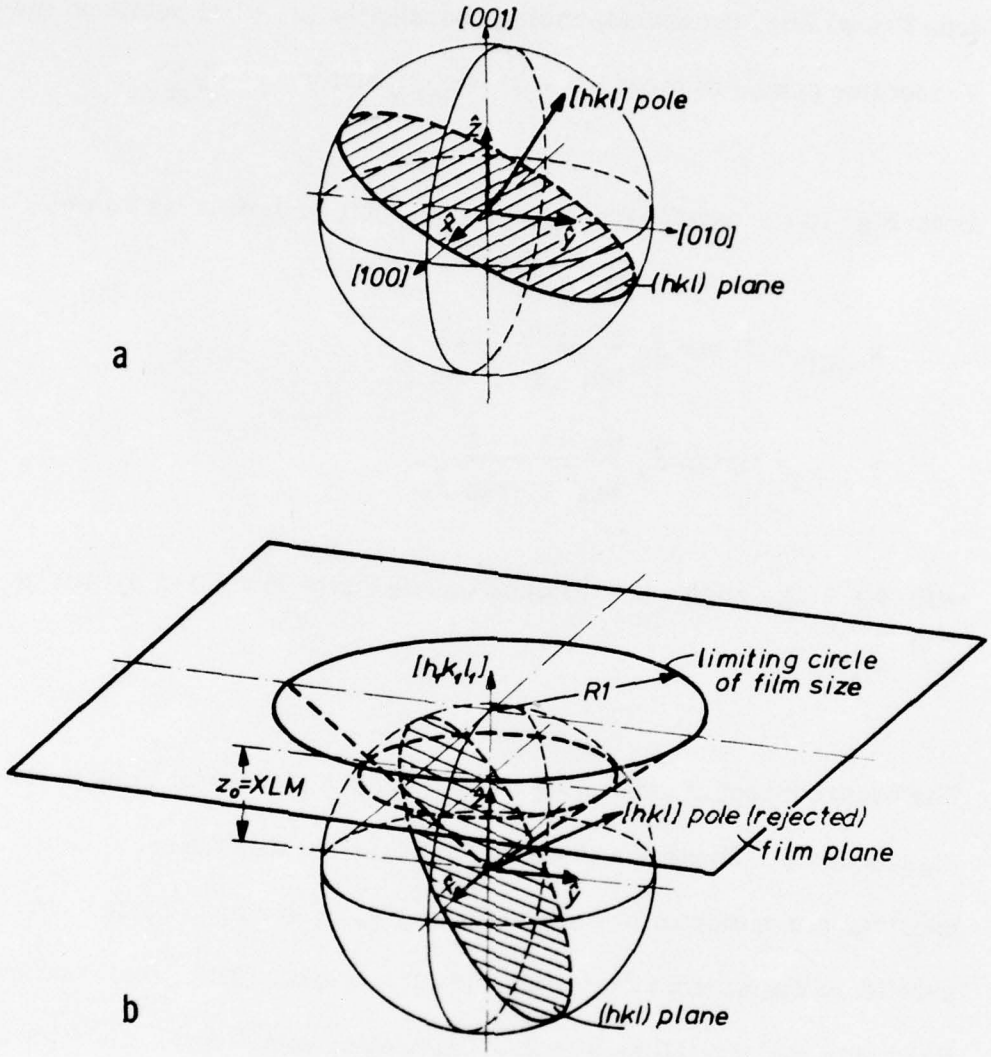

Fig. 2. Geometry a) for calculating coordinates on the projection sphere for all (hkℓ) poles with structure factor $F \neq 0$; standard basis is parallel to cubic basis. b) After rotating the sample to get the desired orientation $(h_1 k_1 \ell_1)$ parallel to the $\hat{z}$-axis. The example of (hkℓ) pole shown in the figure will be rejected by the computer program because the pole intersects the film plane outside the actual film size area.

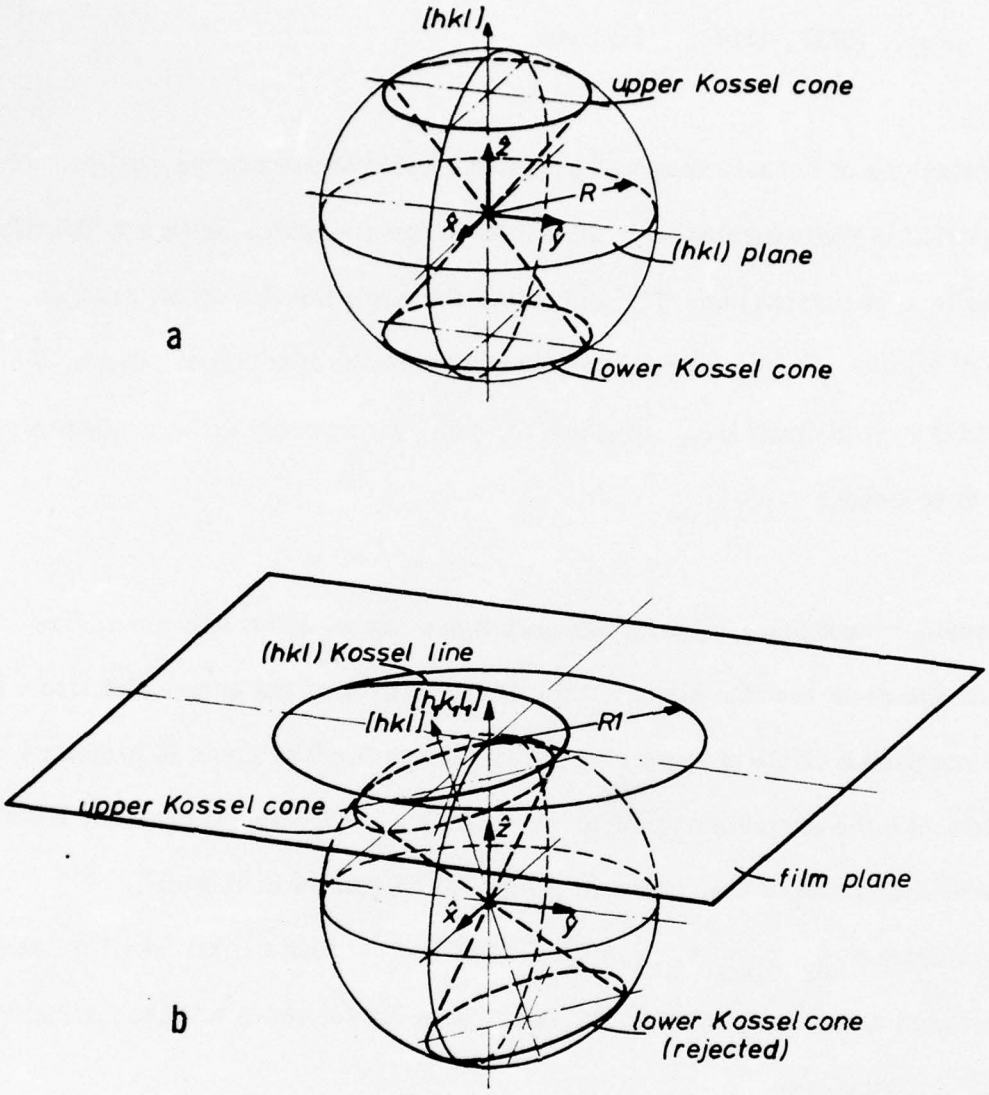

Fig. 3. Geometry a) to generate Kossel cones and to calculate the array of 180 coordinates of the intersection of this cone with the projection sphere; b) after rotating the sample with the desired orientation parallel to the $\hat{z}$-axis. Only that part of the Kossel cone circle is calculated which will be projected within the actual film size area.

2. into a final position for a given crystalline orientation of the sample, e.g., (001), (110), (111), etc.

Intersections of Kossel cones and projection spheres are always circles. The projection of these circles from the center of the projection sphere to the film plane is then carried out. Through this procedure the circles on the sphere transform into circles, ellipses or hyperbolas in the film plane. (Here, if Kikuchi and/or channeling maps are desired, the stereographic projection has to be used.)

To avoid unnecessary calculations only those Kossel cones are considered which intersect the film plane within the small area of the actual film size. For this purpose a circle of approximate film size in the film plane is projected backwards onto the projection sphere. A limiting z_o-value by the constant z-coordinate of each point of the projected circle on the sphere is obtained. Then the coordinates $x_{hk\ell}$, $y_{hk\ell}$, $z_{hk\ell}$ of the pole of the net plane (hkℓ) intersecting the projection sphere are calculated. Only those Kossel cones are considered where $z_{hk\ell} > z_o$ (Fig. 2b).

Figure 3 shows how Kossel lines are obtained. We start with the cubic basis in a position where (hkℓ) is parallel to the z-axis of the standard basis. In this position the Kossel cone of the corresponding set of net-planes (hkℓ) intersects the projection sphere in two planes parallel to the x-y plane of the standard basis. The intersecting lines are circles. The z-coordinates of each point on the circle

has the same value ZZ (1) or ZZ (2) for the top or bottom circle respectively. After rotating the crystal with reference to the standard basis in order to get the desired orientation (h_1, k_1, ℓ_1) parallel to the z-axis, we obtain new coordinates (x_c, y_c, z_c) of the circle points. Once again a check is made as to whether parts of the circle will come into the photographic film area by comparing z_c with the limiting value z_o. The part of the circle with $z_c > z_o$ will be projected into the film plane and this results in new coordinates (x'_p, y'_p) of the Kossel line. To obtain the pseudo-Kossel pattern the shift (x_{shift}, y_{shift}) as mentioned above is added to the (x'_p, y'_p) coordinates.

THE PROGRAM

The program is written in FORTRAN IV for an IBM 1800 Computer.

Input data

1. Position (u, v, w) of the atoms in the unit cell and the lattice parameter a_o of the investigated sample
2. Radius R of the projection sphere
3. Distances, sample-film DF and source-sample DS, where R = DF + DS
4. Approximate film size $2X_o$ x $2Y_o$
5. Wavelength λ (LAMB) of the x-ray source used in the camera
6. Sample orientation ($h_1 k_1 \ell_1$) = (IX1, IX2, IX3)

Program Steps

1. Structure Factor

The structure factor F is calculated by

$$F^2 = \Sigma \cos^2 2\pi(uh + vk + wl) + \sin^2 2\pi (uh + vk + wl)$$

for each set of net planes $(hk\ell)$.

2. Bragg Angle

The Bragg angle θ for each set of net planes $[hk\ell]$ with structure factor $F \neq 0$ is calculated by the Bragg Equation.

3. Pole Coordinates on Projection Sphere

The coordinates (XHS, XKS, XLS) of the intersection of the plane normal $[hk\ell]$ with the projection sphere are calculated for the cubic basis [(100), (010), (001)] parallel to the standard basis $(\hat{x}, \hat{y}, \hat{z})$. Then the crystal is rotated so that the desired orientation (IX1, IX2, IX3) is parallel to $(\hat{x}, \hat{y}, \hat{z})$. The transformation is carried out by

$$\begin{pmatrix} XH \\ XK \\ XL \end{pmatrix} = \begin{pmatrix} h_1/\sqrt{s_1} & k_1/\sqrt{s_1} & 1_1/\sqrt{s_1} \\ h_2/\sqrt{s_2} & k_2/\sqrt{s_2} & 1_2/\sqrt{s_2} \\ h_3/\sqrt{s_3} & k_3/\sqrt{s_3} & 1_3/\sqrt{s_3} \end{pmatrix} \begin{pmatrix} XHS \\ XKS \\ XLS \end{pmatrix}$$

with $s_i = h_i^2 + k_i^2 + 1_i^2$.

Thus (XH, XK, XL) are the coordinates of the plane normal $[hk\ell]$ intersecting the projection sphere for the final desired orientation of the crystal in reference to the standard basis. Only net planes where $XL > XLM = z_o$ are considered further on.

4. Coordinates of Kossel Cone on the Projection Sphere

a. The crystalline sample is rotated in a position that [hkℓ] is parallel to the $\hat{z}$-axis of the standard basis. The coordinates (XXC, YYC) of the Kossel cone intersection with the projection sphere are calculated in 180 steps of 2^{o} making a complete circle. The x-coordinate is a constant value ZZ (1) for the top circle and ZZ (2) for the bottom circle.

b. The crystal is rotated so that the desired orientation (IX1, IX2, IX3) is parallel to ($\hat{x}$). For this transformation both the matrix mentioned in 3 and the inversed matrix have to be used. An array of coordinates [XCI (KK), YCI (KK), ZCI (KK)] for the 180 circle points is obtained. A check is made to determine which part of the circle will be plotted as a Kossel line within the plotting area by comparing the coordinate ZCI (KK) with the limiting z_D-value XLM.

5. Projection onto the Film Plane

The projection onto the film plane gives a two-dimensional array [XP (J), YP (J)] for the Kossel line to be plotted.

XP (J) = XCI (KK) x R/ZCI (KK) - XSHI

YP (J) = YCI (KK) x R/ZCI (KK) - YSHI

XSHI = YSHI = 0 in case of true Kossel lines.

6. Plotting Section

The Kossel or pseudo-Kossel lines are drawn. At the end of each line the (hkℓ) value is plotted for line identification purposes.

RESULTS

Examples of computer generated Kossel pattern for GaAs with [001], [110], and [111] surface orientation are shown in Figs. 4, 5 and 6 respectively. CuK_α radiation with a wavelength of $\lambda = 1.54051$ Å is used in all cases. The pattern in Fig. 4 is true Kossel pattern (with the exception that the characteristic x-rays of GaAs are not used) with DF = R = 2.63 cm between sample surface and film plane. Figures 5 and 6 show pseudo-Kossel pattern. The original computer generated map is reduced in size by about a factor of two. Figure 7a shows a real pseudo-Kossel pattern as obtained in a Kossel camera. Figure 7b shows the corresponding computer generated pattern. This plot is a best fit to the photographic pattern. The camera parameters were not known before but could be determined to be DF = 2.45 cm and DS = 0.1 cm. The asymmetry of the pattern is caused by a slight deviation of the [001] sample orientation from the z-axis. The best fit in this respect could be obtained when the [3 1 60] direction is parallel to the z-direction. Finally, to get approximately the same pattern by computer simulation as was obtained experimentally by the Kossel camera, the lattice parameter of the sample under investigation had to be changed by 0.1% from 5.6435 Å to 5.6491 Å. No additional matching was necessary for this sample.

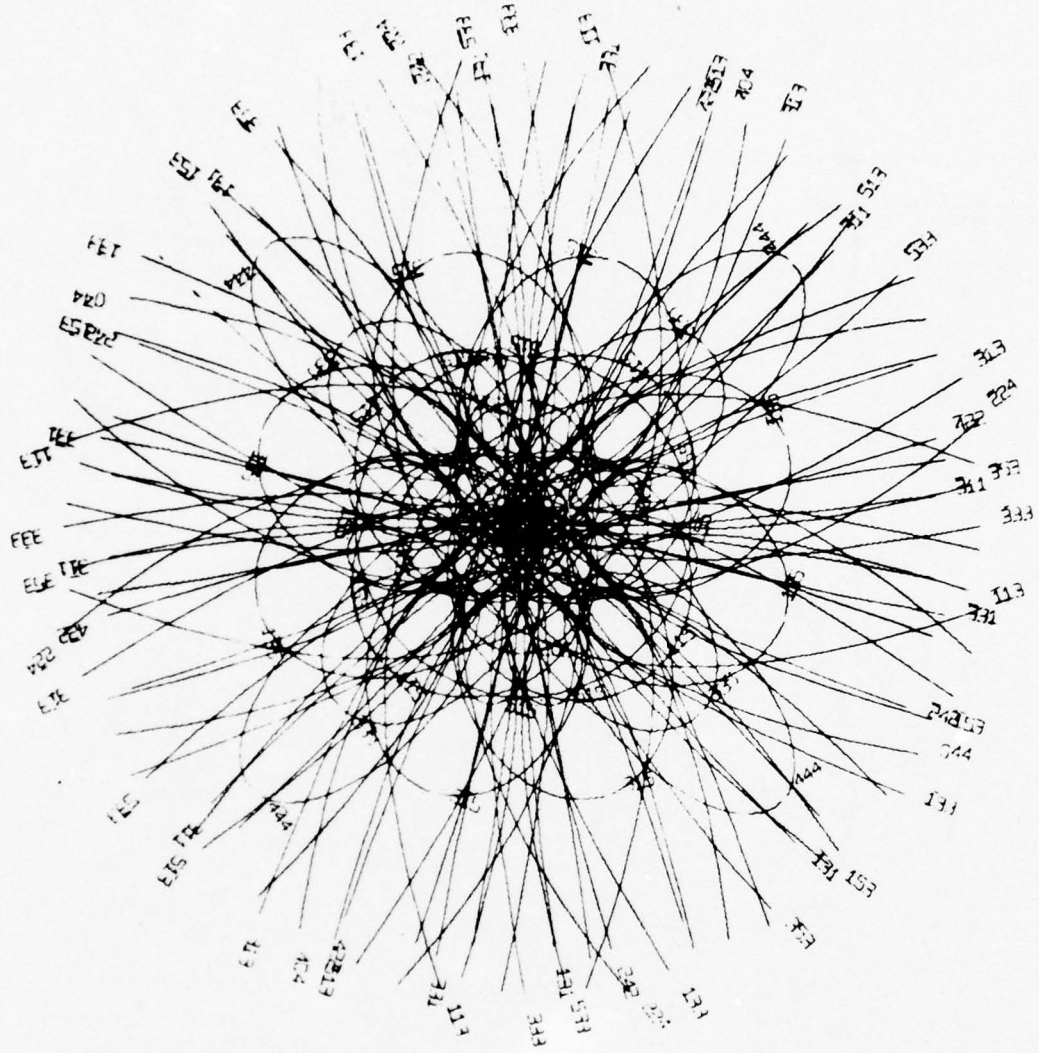

Fig. 4. Example of a computer-generated Kossel pattern for GaAs with surface orientation [001]. The distance between sample and film plane is DF = R = 2.63 cm for this plot.

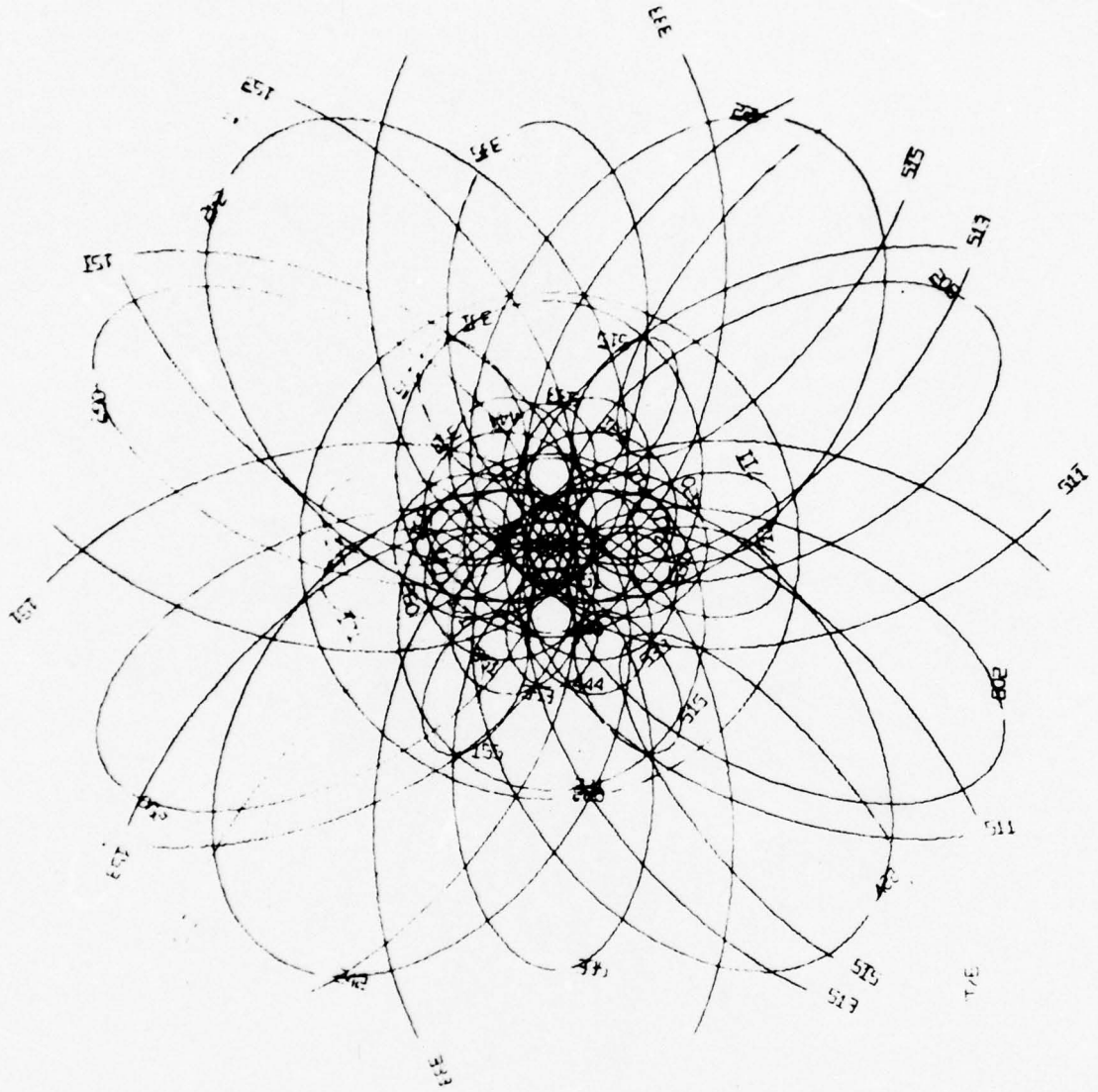

Fig. 5. Example of a computer-generated pseudo-Kossel pattern of a GaAs sample with surface orientation [110]. DF = 2.45 cm and DS = 0.1 cm.

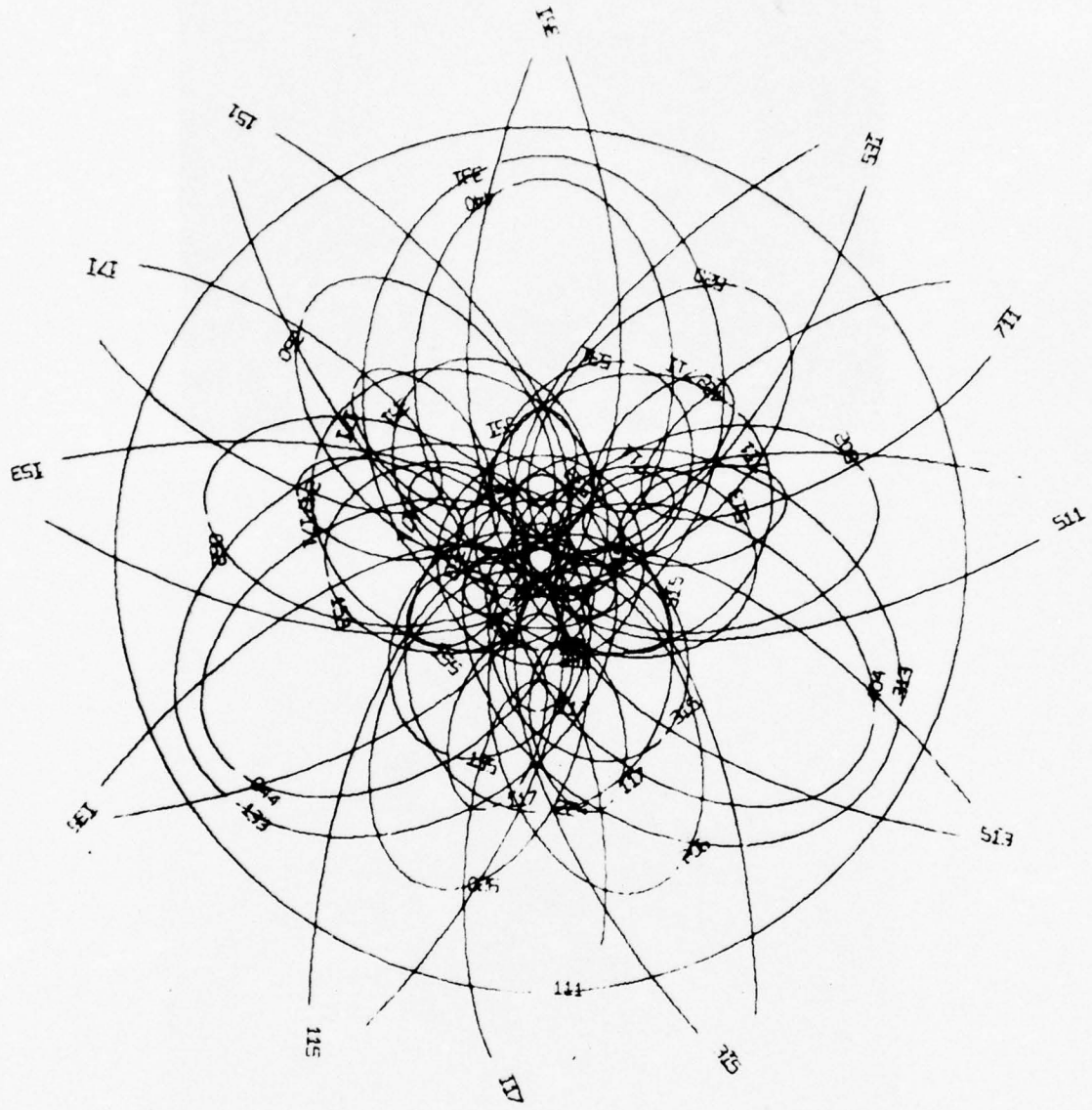

Fig. 6. Example of a computer generated pseudo-Kossel pattern of a GaAs sample with surface orientation [111]. This map was plotted by using the attached FORTRAN IV program for an IBM 1800 computer.

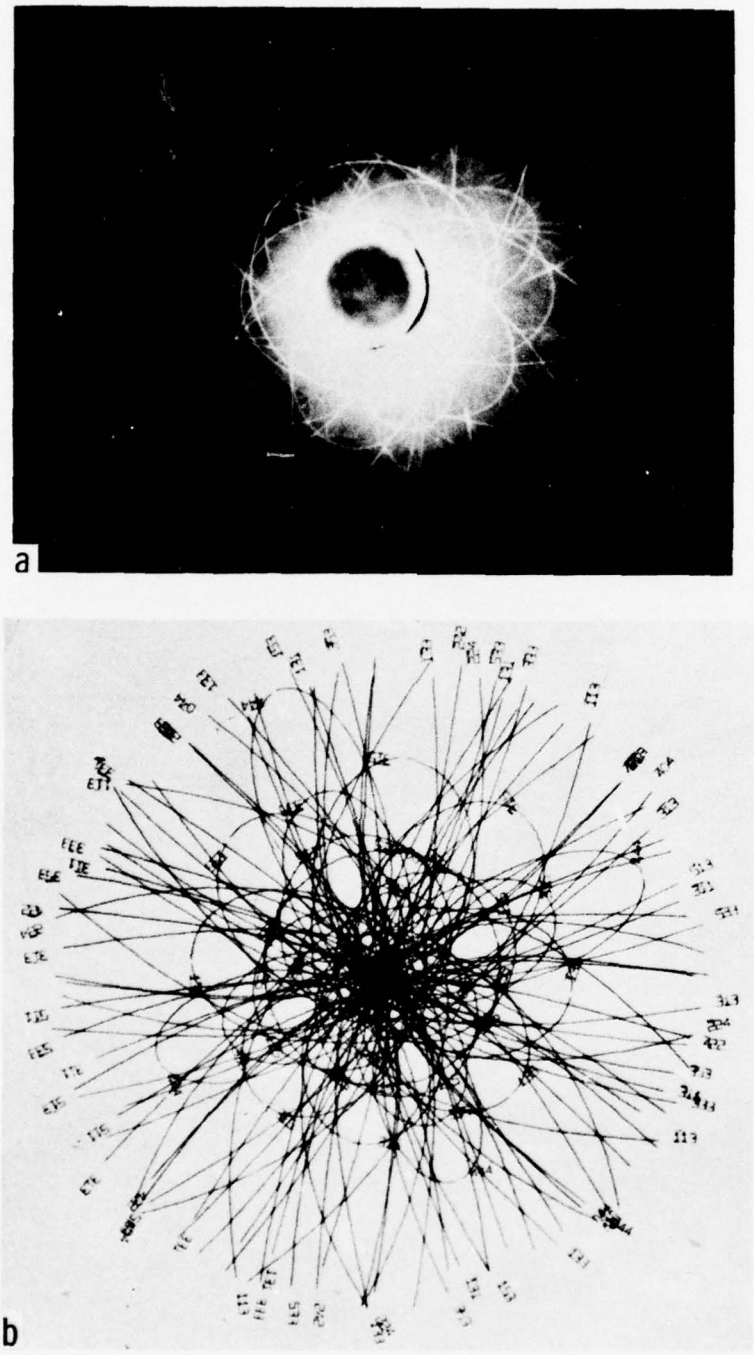

Fig. 7. a) Actual photograph of a pseudo-Kossel pattern of [001] GaAs.
b) Computer plot fitted to the photograph in a). The best fit was found with DF = 2.45 cm, DS = 0.2 cm, surface orientation [3 1 60] close to [001] and lattice parameter a_o = 5.6491 Å, a value 0.1% larger than the tabulated value.

The following experience was obtained during such fitting experiments:

1. Influences on the Kossel line arrangement from different parameters (e.g., distance source-sample or lattice parameter) could well be distinguished.
2. An absolute lattice parameter measurement with an accuracy of 10^{-4} now appears possible by recording just one experimental Kossel pattern instead of the otherwise necessary multiple exposures with varying camera parameters (1, 4). The precision is obtained by fitting experimental Kossel patterns with computer generated maps.

ACKNOWLEDGEMENT

The author would like to thank Ron Anderson for this assistance in operating the IBM 1800 computer and for many discussions.

REFERENCES

1. T. Ellis et al., J. Appl. Phys. 35, 3364, 1964.

2. J. J. Slade et al., J. Appl. Phys. 35, 3373, 1964.

3. L. F. Donghey and R. H. Bissinger, J. Electr. Mat. 4, 131, 1975.

4. S. Weissmann, "Structure-Sensitive Properties of Materials Disclosed by a Combination of X-Ray Topography, X-Ray Diffraction Analysis, and Electron Microscopy Methods," Special Technical Publication 557, American Society for Testing and Materials.

5. C. T. Young and J. L. Lytton, J. Appl. Phys. 43, 1408, 1972.

6. H. F. Kappert, "Computer Generation of Kikuchi Maps for Transmission Electron Microscopy (TEM) and Scanning Electron Microscopy (SEM) Investigations," ARPA Technical Report No. 6, edited by G. H. Schwuttke, July 1975, Contract No. F19628-75-C-0174.

APPENDIX

Program in FORTRAN IV for IBM 1800 Computer

PAGE 0001

```
C
C  GENERATE KOSSEL AND PSEUDO-KOSSEL PATTERN
C
C
*IOCS(CARD, 1443 PRINTER)
*IOCS (PLOTTER)
*TRANSFER TRACE
*ARITHMETIC TRACE
*LIST ALL
*ONE WORD INTEGERS
      INTEGER H,H1,H1A,HA                                          KIKU0000
      REAL LAMB
      DIMENSION U(8),V(8),W(8),SF(9,9,9),XP(180),YP(180),ZZ(2),    KOSS0001
     1XC1(180),YC1(180),ZC1(180),XC2(180),YC2(180),ZC2(180)        KOSS0002
C
C  READ LATTICE PARAMETER
C
      DO 10 I=1,8                                                  KIKU0010
      READ (2,7) U(I),V(I),W(I)                                    KIKU0012
    7 FORMAT (3F6.2)                                               KIKU0014
   10 CONTINUE                                                     KIKU0016
C
C
C   R IS RADIUS OF STERO SPHERE
C
      DF=2.45                                                      KOSS0019
      DS=0.1                                                       KOSS0020
      R=DF+DS                                                      KOSS0021
C
C  R1=RADIUS OF PLOTTING CIRCLE, XO,YO PLOTTING SQUARE
C
      XO= 9.                                                       KOSS0023
      YO= 9.                                                       KOSS0024
      R1=SQRT(XO*XO+YO*YO)                                         KIKU0025
C
      THEM=ATAN(R1/R)                                              KOSS0030
      XLM=R*COS(THEM)                                              KOSS0035
C   PRODUCE (H,K,L) VALUES
C
      DO 19 H=1,9                                                  KIKU0050
      H1=H-1                                                       KIKU0051
      DO 29 K=1,9                                                  KIKU0060
      K1=K-1                                                       KIKU0061
      DO 39 L=1,9                                                  KIKU0070
      L1=L-1                                                       KIKU0071
C
C  CALCULATE STRUCTURFACTOR
C
      F1=0.0                                                       KIKU0080
      F2=0.0                                                       KIKU0085
      THET=0.0                                                     KIKU0090
      DO 50 M=1,8                                                  KIKU0095
      A=6.28*(U(M)*H1+V(M)*K1+W(M)*L1)                             KIKU0100
      F1=F1+COS(A)                                                 KIKU0105
      F2= F2+SIN(A)                                                KIKU0106
   50 CONTINUE                                                     KIKU0107
      F=ROUND(F1**2+F2**2)                                         KIKU0110
      SF(H,K,L)=F                                                  KIKU0117
   39 CONTINUE                                                     KIKU0118
```

```
   29 CONTINUE                                                          KIKU0119
   19 CONTINUE                                                          KIKU0120
      XSCAL=3.33                                                        KIKU5207
      YSCAL=XSCAL                                                       KIKU5208
      CALL SCALF (XSCAL,YSCAL,0.0,0.0)                                  KOSS0122
      DO 20 H=1,17                                                      KIKU0123
      H1=H-9                                                            KIKU0123
      H1A=IABS(H1)+1                                                    KOSS0124
      DO 30 K=1,17                                                      KIKU0125
      K1=K-9                                                            KIKU0125
      K1A=IABS(K1)+1                                                    KIKU0126
      DO 40 L=1,17                                                      KIKU0127
      L1=L-9                                                            KIKU0127
      L1A=IABS(L1)+1                                                    KIKU0128
      F=SF(H1A,K1A,L1A)                                                 KIKU0129
      IF(F-1.)  40,40,60                                                KIKU0190
   60 SQ=SQRT(FLOAT(H1*H1+K1*K1+L1*L1))
C
C  BRAGG ANGLE X-RAY LAMBDA=1.54051AE, GA AS  A=5.6435 AE
C
      LAMB=1.54051                                                      KOSS0191
      AO=5.6491                                                         KOSS0192
      THE=SQ*(LAMB/(2.*AO))                                             KOSS0193
      IF(THE-1.) 65,40,40                                               KOSS0193
   65 ET=THE/SQRT(1.-THE*THE)                                           KOSS0194
      THET=ATAN(ET)                                                     KOSS0195
C
C
C SELECCT PLANES OF HIGHER INDEX THAN SMSQ
C
      SMSQ=1.5                                                          KOSS0200
      IF(SMSQ-SQ) 140,140,40                                            KIKU0205
C
C  CALCULATE COORDINATES ON STEREO SPHERE
C
C  FOR POL (H1,K1,L1)
C
  140 IF (SQ-0.5) 40,40,141                                             KIKU0300
  141 XHS=R*H1/SQ                                                       KIKU0305
      XKS=R*K1/SQ                                                       KIKU0310
      XLS=R*L1/SQ                                                       KIKU0320
C
C  TRANSITION TO DESIRED ORIENTATION WITH COORD. IX1,IX2,IX3
C
      IX1=1                                                             KOSS0361
      IX2=1                                                             KOSS0362
      IX3=1                                                             KOSS0363
      X1=FLOAT(IX1)                                                     KOSS0364
      X2=FLOAT(IX2)                                                     KOSS0365
      X3=FLOAT(IX3)                                                     KOSS0366
      Q=SQRT(X1*X1+X2*X2+X3*X3)                                         KOSS0365
      X31=X1/Q                                                          KOSS0366
      X32=X2/Q                                                          KOSS0367
      X33=X3/Q                                                          KOSS0368
      QX=SQRT(X31*X33*X31*X33+X32*X33*X32*X33+X32**4.+X31**4.+          KOSS0369
     22.*X32*X32*X31*X31)                                               KOSS0370
      QY=SQRT(X32*X32+X31*X31)                                          KOSS0371
      IF(QY-0.5)123,123,122                                             KOSS0372
  122 X11=-X31*X33/QX                                                   KOSS0374
```

```
      X12=-X32*X33/QX                                                   KOSS0375
      X13=(X32*X32+X31*X31)/QX                                          KOSS0376
      X21=X32/QY                                                        KOSS0377
      X22=-X31/QY                                                       KOSS0378
      X23=0.                                                            KOSS0379
      GO TO 125                                                         KOSS0380
  123 X11=1.0                                                           KOSS0381
      X12=0.                                                            KOSS0382
      X13=0.                                                            KOSS0383
      X21=0.                                                            KOSS0384
      X22=1.                                                            KOSS0385
      X23=0.                                                            KOSS0386
  125 S1=SQRT(X11*X11+X12*X12+X13*X13)                                  KIKU0371
      S2=SQRT(X21*X21+X22*X22+X23*X23)                                  KIKU0372
      S3=SQRT(X31*X31+X32*X32+X33*X33)                                  KIKU0372
      A11=X11/S1                                                        KIKU0375
      A12=X12/S1                                                        KIKU0376
      A13=X13/S1                                                        KIKU0377
      A21=X21/S2                                                        KIKU0378
      A22=X22/S2                                                        KIKU0379
      A23=X23/S2                                                        KIKU0380
      A31=X31/S3                                                        KIKU0381
      A32=X32/S3                                                        KIKU0382
      A33=X33/S3                                                        KIKU0383
      XH=A11*XHS+A12*XKS+A13*XLS                                        KIKU0385
      XK=A21*XHS+A22*XKS+A23*XLS                                        KIKU0386
      XL=A31*XHS+A32*XKS+A33*XLS                                        KIKU0387
C
C  XSHI,YSHI=SHIFT OF KOSSEL ELLIPSE FOR PSEUDO KOSSEL PATTERN
C
      ET2=ET*ET                                                         KOSS0388
      XHL=XH/XL                                                         KOSS0388
      XKL=XK/XL                                                         KOSS0388
      XSHI=(2.*XH*DS/XL)*((ET2+1.)/(ET2-XHL))                           KOSS0388
      YSHI=(2.*XK*DS/XL)*((ET2+1.)/(ET2-XKL))                           KOSS0389
      IF(XL-XLM) 40,40,130                                              KOSS0390
C
C  REJECT PLANES OF HIGHER ORDER
C
  130 XI1=10000.*(H1A-1)+100.*(K1A-1)+(L1A-1)                           KIKU0390
      DO 80 IH=1,5                                                      KIKU0391
      IH1=IH-1                                                          KIKU0392
      DO 80 IK=1,5                                                      KIKU0393
      IK1=IK-1                                                          KIKU0394
      DO 100 IL=1,5                                                     KIKU0395
      IL1=IL-1                                                          KIKU0396
      IF(IH1+IK1+IL1) 100,100,101                                       KIKU0397
  101 DO 110 N=2,8                                                      KIKU0398
      XI2=N*(10000.*IH1+100.*IK1+IL1)                                   KIKU0399
      RDXI=XI1-XI2                                                      KIKU0400
      ARDX=ABS(RDXI)                                                    KIKU0402
      IF(ARDX-0.1) 45,45,46                                             KIKU0403
   46 IF(RDXI) 100,45,110                                               KIKU0404
   45 DO 111 M=1,8                                                      KIKU0406
      IH5=IH1*M+1                                                       KIKU0407
      IK5=IK1*M+1                                                       KIKU0408
      IL5=IL1*M+1                                                       KIKU0409
      IG=IH1+IK1+IL1                                                    KIKU0410
      IF (IG) 111,111,43                                                KIKU0411
```

```
   43 FH=SF(IHS,IKS,ILS)                                                KIKU0412
      IF(FH-1.) 111,111,41                                              KIKU0413
  111 CONTINUE                                                          KIKU0415
   41 RN=FLOAT (N)                                                      KIKU0416
      RM=FLOAT(M)                                                       KIKU0417
      RMN=ROUND(RN/RM)                                                  KIKU0418
      IF(RMN-4.) 252,252,40                                             KIKU0419
  110 CONTINUE                                                          KIKU0420
  100 CONTINUE                                                          KIKU0421
   90 CONTINUE                                                          KIKU0422
   80 CONTINUE                                                          KIKU0425
C
C  COORDINATES FOR DIFFR.CONE ON SPHERE
C
  252 S=SIN(THET)                                                       KOSS0500
      C=COS(THET)                                                       KOSS0510
      RP=R*C                                                            KOSS0520
      ZZ(1)=R*S                                                         KOSS0530
      ZZ(2)=-R*S                                                        KOSS0540
      SQX=SQRT(XHS*XLS*XHS*XLS+XKS*XLS*XKS*XLS+XKS**4.+XHS**4.+2.*XKS   KOSS0600
     2*XKS*XHS*XHS)                                                     KOSS0601
      SQY=SQRT(XKS*XKS+XHS*XHS)                                         KOSS0610
      IF(SQY-0.5) 143,143,142                                           KOSS0612
  142 XX11=-XHS*XLS/SQX                                                 KOSS0615
      XX12=-XKS*XLS/SQX                                                 KOSS0620
      XX13=( XKS*XKS+XHS*XHS)/SQX                                       KOSS0625
      XX21=XKS/SQY                                                      KOSS0630
      XX22=-XHS/SQY                                                     KOSS0635
      XX23=0.                                                           KOSS0640
      GO TO 145                                                         KOSS0641
  143 XX11=1.                                                           KOSS0643
      XX12=0.                                                           KOSS0643
      XX13=0.                                                           KOSS0643
      XX21=0.                                                           KOSS0643
      XX22=1.                                                           KOSS0643
      XX23=0.                                                           KOSS0643
  145 XX31=XHS/R                                                        KOSS0645
      XX32=XKS/R                                                        KOSS0650
      XX33=XLS/R                                                        KOSS0655
C
C  TRANSFORMATION TO SYSTEM (001) PARALLEL TO Z-AXIS
C
      SX1=SQRT(XX11*XX11+XX12*XX12+XX13*XX13)                           KOSS0680
      SX2=SQRT(XX21*XX21+XX22*XX22+XX23*XX23)                           KOSS0682
      SX3=SQRT(XX31*XX31+XX32*XX32+XX33*XX33)                           KOSS0685
C
C  MATRIX
C
      AA11=XX11/SX1                                                     KOSS0700
      AA12=XX12/SX1                                                     KOSS0701
      AA13=XX13/SX1                                                     KOSS0702
      AA21=XX21/SX2                                                     KOSS0703
      AA22=XX22/SX2                                                     KOSS0704
      AA23=XX23/SX2                                                     KOSS0705
      AA31=XX31/SX3                                                     KOSS0706
      AA32=XX32/SX3                                                     KOSS0707
      AA33=XX33/SX3                                                     KOSS0708
      D=AA11*AA22*AA33+AA21*AA32*AA13+AA31*AA12*AA23-AA31*AA22*AA13     KOSS0710
     2-AA11*AA32*AA23-AA21*AA12*AA33                                    KOSS0711
```

```
C
C  MATRIX INVERSED
C
      B11=(AA22*AA33-AA23*AA32)/D                                    KOSS0720
      B12=-(AA12*AA33-AA13*AA32)/D                                   KOSS0721
      B13=(AA12*AA23-AA13*AA22)/D                                    KOSS0722
      B21=-(AA21*AA33-AA23*AA31)/D                                   KOSS0723
      B22=(AA11*AA33-AA13*AA31)/D                                    KOSS0724
      B23=-(AA11*AA23-AA13*AA21)/D                                   KOSS0725
      B31=(AA21*AA32-AA22*AA31)/D                                    KOSS0726
      B32=-(AA11*AA32-AA12*AA31)/D                                   KOSS0727
      B33=(AA11*AA22-AA12*AA21)/D                                    KOSS0728
      BET1=1.570796-THET                                             KOSS0730
      BE=XL/SQRT(R*R-XL*XL)                                          KOSS0732
      BET2=ATAN(BE)                                                  KOSS0734
      BET3=BET2-BET1                                                 KOSS0736
      ZM=R*SIN(BET3)                                                 KOSS0738
      DO 500 I=1,2                                                   KOSS0750
      J=0                                                            KOSS0755
      DO 600 M=2,360,2                                               KOSS0760
      KK=M/2                                                         KOSS0765
      PH=M*3.141593/180.                                             KOSS0770
C
C  COORD OF KOSS CONE,(HKL) PARALLEL TO Z-AXIS
C
      XXC=RP*COS(PH)                                                 KOSS0780
      YYC=RP*SIN(PH)                                                 KOSS0785
C
C  COORD OF KOSS CONE,(001) PARALLEL TO Z-AXIS
C
      XC=B11*XXC+B12*YYC+B13*ZZ(I)                                   KOSS0800
      YC=B21*XXC+B22*YYC+B23*ZZ(I)                                   KOSS0802
      ZC=B31*XXC+B32*YYC+B33*ZZ(I)                                   KOSS0804
C
C  COORD OF KOSS CONE,WANTED CENTER POLE PARALLEL TO Z-AXIS
C
      XC1(KK)=A11*XC+A12*YC+A13*ZC                                   KOSS0820
      YC1(KK)=A21*XC+A22*YC+A23*ZC                                   KOSS0822
      ZC1(KK)=A31*XC+A32*YC+A33*ZC                                   KOSS0824
      IF((ZC1(KK)-ZM)-0.01) 550,550,600                              KOSS0830
  550 KK0=KK                                                         KOSS0832
      KK1=KK0+1                                                      KOSS0834
  600 CONTINUE                                                       KOSS0840
      DO 601 KK=1,KK0                                                KOSS0841
      K3=180-KK0+KK                                                  KOSS0842
      XC2(K3)=XC1(KK)                                                KOSS0843
      YC2(K3)=YC1(KK)                                                KOSS0844
      ZC2(K3)=ZC1(KK)                                                KOSS0845
  601 CONTINUE                                                       KOSS0846
      DO 602 KK=KK1,180                                              KOSS0847
      K4=KK-KK0                                                      KOSS0847
      XC2(K4)=XC1(KK)                                                KOSS0848
      YC2(K4)=YC1(KK)                                                KOSS0848
      ZC2(K4)=ZC1(KK)                                                KOSS0848
  602 CONTINUE                                                       KOSS0849
      DO 603 KK=1,180                                                KOSS0850
      IF(ZC2(KK)-XLM) 603,603,580                                    KOSS0852
  580 J=J+1                                                          KOSS0855
C
```

```
C  COORD OD KOSS CONE IN PROJECTION PLANE                                KOSS0860
C                                                                       KOSS0865
      XP(J)=XC2(KK)*R/ZC2(KK)-XSHI                                      KOSS0870
      YP(J)=YC2(KK)*R/ZC2(KK)-YSHI
  603 CONTINUE
C
C  PLOTTING SECTION                                                     KOSS5200
C                                                                       KIKU5210
      IF(J-140) 500,699,699                                             C
  699 CALL FPLOT (-2,XP(1),YP(1))                                       KIKU5220
      WRITE(5,6962) H,K,L                                               KIKU5230
 6962 FORMAT (8X,3I3)                                                   KIKU5240
      DO 700 JJ=1,J                                                     KIKU5312
  700 CALL FPLOT (0,XP(JJ),YP(JJ))                                      KOSS5310
      CALL FPLOT (-1,XP(J),YP(J))                                       KIKU5314
      DX=XP(J)-XP(J-2)                                                  KIKU5316
      DY=YP(J)-YP(J-2)                                                  KIKU5318
      IF(DX) 7012,7011,7010                                             KIKU5320
 7010 DEL=ATAN(DY/DX)                                                   KIKU5328
      GO TO 7020                                                        KIKU5330
 7011 DEL =0.0                                                          KIKU5335
      GO TO 7020                                                        KIKU5340
 7012 DEL=ATAN(DY/DX)+3.141593                                          KIKU5341
 7020 XB=XP(J)+0.5*COS(DEL)                                             KIKU5342
      YB=YP(J)+0.5*SIN(DEL)                                             KIKU5343
      HA=IABS(H1)                                                       KIKU5345
      KA=IABS(K1)                                                       KIKU5350
      LA=IABS(L1)                                                       KIKU5351
      CALL FCHAR(XB,YB,.1,.12,DEL)                                      KIKU5360
      WRITE(11,7099) HA,KA,LA                                           KIKU5361
 7099 FORMAT (3I1)                                                      KIKU5362
      XB1=XB-0.35*SIN(DEL)                                              KIKU5363
      YB1=YB+0.35*COS(DEL)                                              KIKU5365
      DXB=0.25*COS(DEL)                                                 KIKU5366
      DYB=0.25*SIN(DEL)                                                 KIKU5367
      XB2=XB1+DXB                                                       KIKU5368
      YB2=YB1+DYB                                                       KIKU5369
      XB3=XB1+2.*DXB                                                    KIKU5370
      YB3=YB1+2.*DYB                                                    KIKU5372
      XB4=XB1+3.*DXB                                                    KIKU5374
      YB4=YB1+3.*DYB                                                    KIKU5375
      IF(H1) 7061,7060,7060                                             KIKU5376
 7061 CALL FPLOT(-2,XB1,YB1)                                            KIKU5377
      CALL FPLOT (-1,XB2,YB2)                                           KIKU5378
 7060 IF(K1) 7071,7070,7070                                             KIKU5379
 7071 CALL FPLOT(-2,XB2,YB2)                                            KIKU5380
      CALL FPLOT(-1,XB3,YB3)                                            KIKU5381
 7070 IF(L1)7081,500,500                                                KIKU5300
 7081 CALL FPLOT(-2,XB3,YB3)                                            KIKU5400
      CALL FPLOT(-1,XB4,YB4)                                            KIKU5500
  500 CONTINUE                                                          KIKU5600
   40 CONTINUE                                                          KOSS5800
   30 CONTINUE                                                          KOSS5810
   20 CONTINUE                                                          KOSS5820
      CALL FCHAR(12.,12.,.1,.12,0.)                                     KOSS5825
      WRITE(11,8001) IX1,IX2,IX3                                        KOSS5830
 8001 FORMAT (3I3,'  POLE')
      CALL FCHAR(12.,11.,.1,.12,0.)
      WRITE(11,8002)
```

```
 8002 FORMAT ('KOSSEL PATTERN')                                          KOSS5935
      CALL CNVDT(J4,JD,JY)                                               KOSS5946
      CALL FCHAR(10.,10.,.1,.12,0.)                                      KOSS5940
      WRITE(11,8003) JM,JD,JY                                            KOSS5945
 8003 FORMAT(I2,'/',I2,'/',I4)                                           KOSS5950
      CALL FCHAR(12.,-10.,.1,.12,0.)                                     KOSS5955
      WRITE(11,8004) DF, LAMB                                            KOSS5960
 8004 FORMAT('DF=',F5.2,'CM',2X,'LAMBDA=',F8.5)                          KOSS5965
      CALL FCHAR(12.,-11.,.1,.12,0.)                                     KOSS5970
      WRITE(11,8005) DS,A0                                               KOSS5975
 8005 FORMAT('DS=',F5.2,'CM',6X,'A0=',F8.5)                              KOSS5980
      CALL FCHAR(12.,-12.,.1,.12,0.)                                     KOSS5985
      WRITE(11,8006) R                                                   KOSS5990
 8006 FORMAT(' R=',F5.2,'CM',2X,'RUN NO.')                               KOSS5995
      CALL EXIT
      END
*CCEND
  0.00  0.00  0.00
  0.50  0.50  0.00
  0.50  0.00  0.50
  0.00  0.50  0.50
  0.25  0.25  0.25
  0.75  0.75  0.25
  0.75  0.25  0.75
  0.25  0.75  0.75
```

Chapter 2

IMPACT SOUND STRESSING (ISS) OF GaAs WAFERS

by R. G. Dessauer and E. Hearn

1. INTRODUCTION

Surface damage in covalently bonded crystals is only ill understood. Numerous workers in the field have studied damage in semiconductor crystals caused by grinding, polishing, or lapping.[1] Due to the complexity of damage introduced by these techniques a complete analysis of crystal damage is very difficult. Consequently, the annealing of damage is only partially understood and only few experimental facts to support a cause and effect relationship between original damage and subsequent defect generation are available.

In this context the technique of Impact Sound Stressing (ISS) has become very useful to study mechanical damage in silicon surfaces.[2] This technique has found unique utilization not only in degrading silicon surfaces in a controlled manner -- and thus allowing detailed damage studies -- but also in using mechanical damage, introduced on the wafer backside, to reduce the defect density (stacking faults) in the wafer frontside.

This report describes the application of ISS for GaAs wafers. The intent of this investigation is to develop a technique for III - V compounds capable of introducing, in a controlled manner, damage into crystal surfaces. This will provide a means not only for the study of damage propagation in such crystals, but also for investigation of possibilities of damage gettering in III - V compounds.

2. ISS EQUIPMENT

The Impact Sound Stressing (ISS) technique used for silicon[1] has been adapted for the introduction of microdamage into GaAs surfaces. The brittle nature of the material and the irregular sizes and shapes of wafers mandate certain pertinent process and equipment changes.

The non-circular, non-uniform shape of GaAs single crystal wafers is due to the horizontal zoning growth process. This process is generally used for the production of standard quality material. It results in a single crystal ingot having the shape of the containing boat. The size and shape of wafers cut economically from such an ingot are thus determined by the quantity of material placed in the boat, its shape, and the slicing direction. Non-uniform wafers are

accommodated in the ISS apparatus by mounting them on circular membranes which are then placed into the apparatus.

The flexural stresses induced in the brittle wafers and the mounting material, during ISS, are reduced by placing the sample carrier membrane away from the source of sound. This arrangement protects against wafer breakage and avoids detachment of the samples from the membrane. It permits the convenient use of wax for sample mounting.*

A similar membrane, but without a sample attached, is used as the driver. The driver membrane impels the tungsten balls against the sample mounted on the carrier membrane above, thus producing the microdamage.

2.1 Equipment Description

A schematic representation of the apparatus is given in Fig. 1. A photograph of the actual equipment as in operation is shown in Fig. 2a, with the acoustic enclosure containing the ISS unit to the right of the controls console containing the electronic equipment. An additional view showing the apparatus within the acoustic enclosure is given in Fig. 2b.

---

*Recently, a vacuum system has been successfully used to hold samples on the sample carrier membrane during ISS.

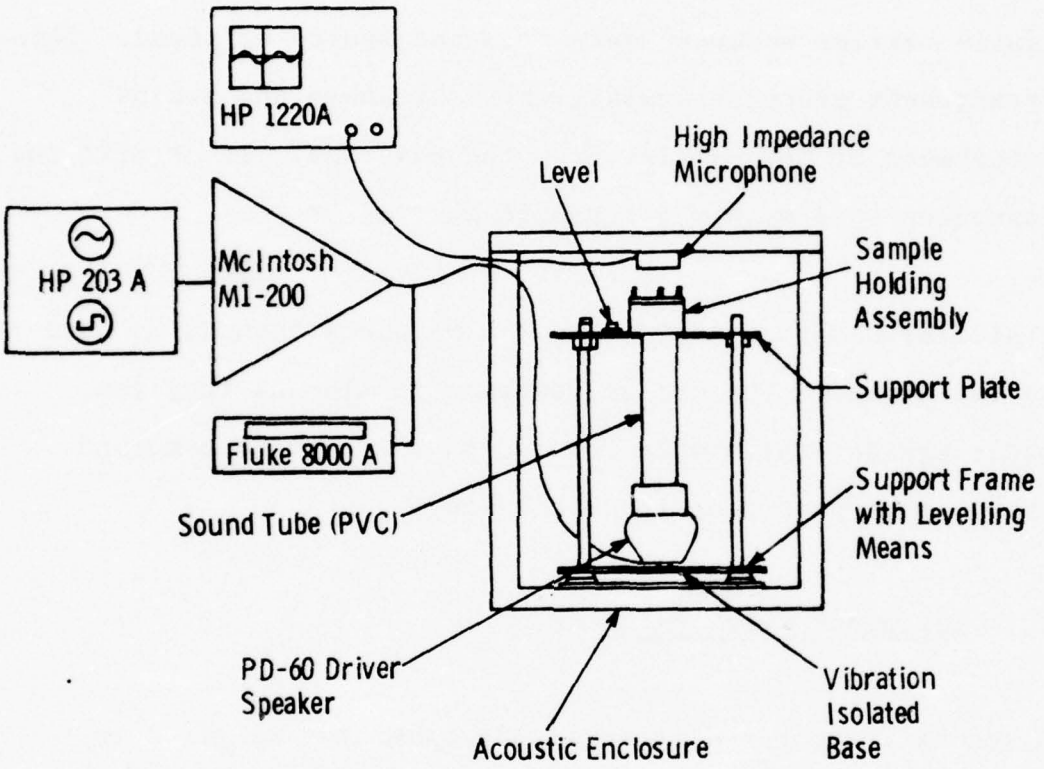

Fig. 1. Schematic of Impact Sound Stressing (ISS) apparatus for GaAs.

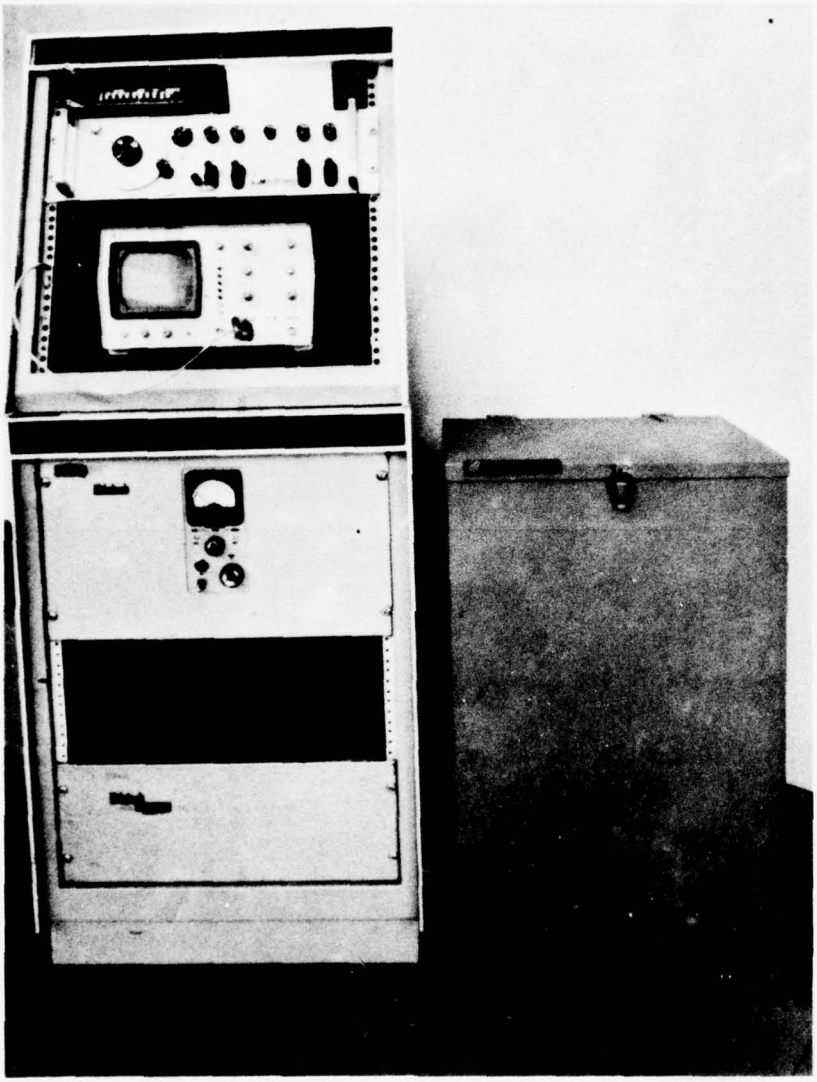

Fig. 2a. Photograph of instrumentation corresponding to Fig. 1 (acoustic enclosure at right).

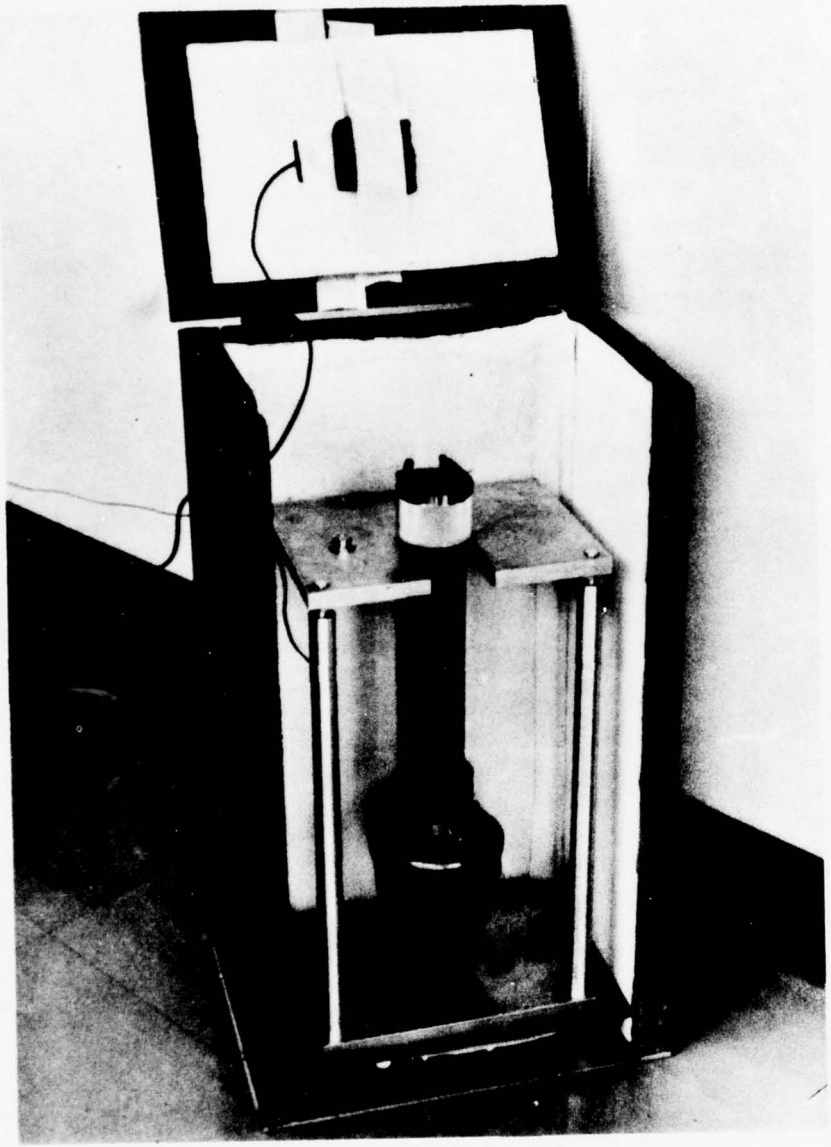

Fig. 2b. Equipment within acoustic enclosure.

The source of sound is the driver portion of a loud-speaker (Atlas Model PD-60T/60 watt), operated by a MacIntosh MI-200 power amplifier. Input power to the acoustic driver is monitored by a Fluke 8000A digital multimeter for coarse setting to avoid overdriving. A Hewlett-Packard HP 203A function generator provides the sinusoidal oscillation. This equipment is also capable of producing square wave pulses.

The sound tube is a polyvinyl chloride (PVC) pipe attached to the driver by a threaded PVC coupling. The sample holder assembly is threaded to the top end of the sound tube. The effective length of tube, coupling the driver membrane in the sample holder assembly to the driver, is approximately 35 cm. The assembled unit is suspended in the support frame. The support plate rests on adjustment nuts threaded on the three symmetrically placed support rods. This three-point suspension is used to level the apparatus. A button type bubble level placed on the support plate serves as level indicator. The support frame rests on a base equipped with four vibration isolators. It is located in the acoustic enclosure which reduces environmental sound to levels acceptable in open laboratory or manufacturing areas. A high impedance microphone, used to monitor the sound emitted at the sample carrier membrane, is installed in the hinged cover of the acoustic enclosure. It is located so that when the cover is closed, the microphone is

positioned directly above the sample holding assembly. Sound attenuating foam rubber is installed on the microphone as needed to avoid overdriving it. The output signal from the microphone is displayed on a Hewlett-Packard HP 1220A oscilloscope.

Repeatable ISS action for different runs is achieved by keeping the displayed amplitude on the oscilloscope constant. This is done by fine adjustment of the input power to the driver at resonant frequency for each run. This monitoring system corrects for the effects of small differences in samples and sample carrier membranes and also neutralizes the effects of resonant frequency changes caused by aging of the driver membrane. Effects of small changes in the effective tube length due to replacement of drivers or other assembly parts are corrected similarly. The oscilloscope also aids in accurately finding the resonant frequency.

A detailed sketch of the sample holding assembly is given in Fig. 3, and a photograph of the actual unit, as in operation, is shown in Fig. 4a. In Fig. 4b the sample carrier clamping ring and membrane have been removed, and the membrane with a sample mounted is displayed above the unit. The tungsten balls are seen resting on the driver membrane.*

---

* The balls are approximately 0.3mm in diameter and, in order to avoid repeated counting, several quantities were weighed. Figure 5 shows the correlation of weight to the number of balls. The slope of the line gives the weight of one ball. This graph may be used to weigh out the correct number of balls to within $\pm$ 0.05%.

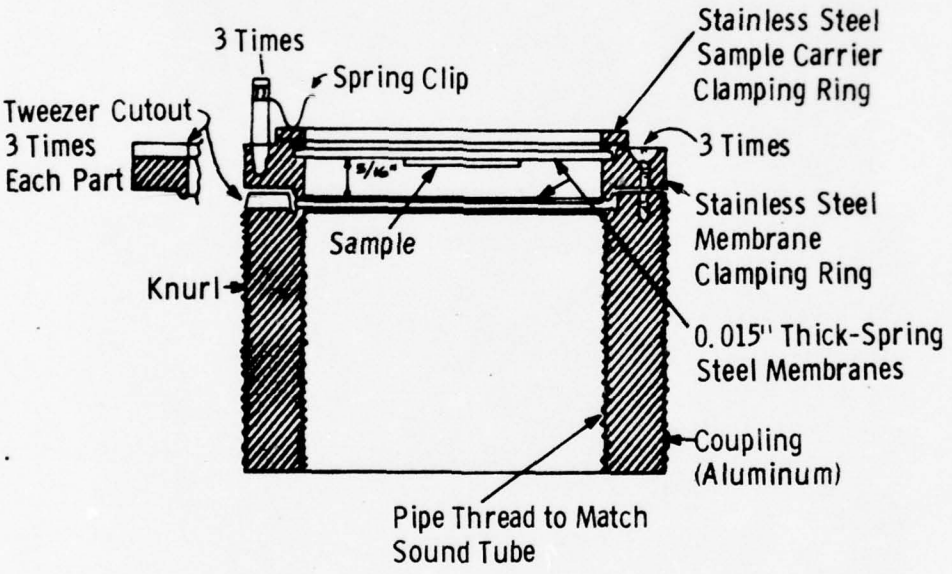

Fig. 3. GaAs sample holding assembly for ISS.

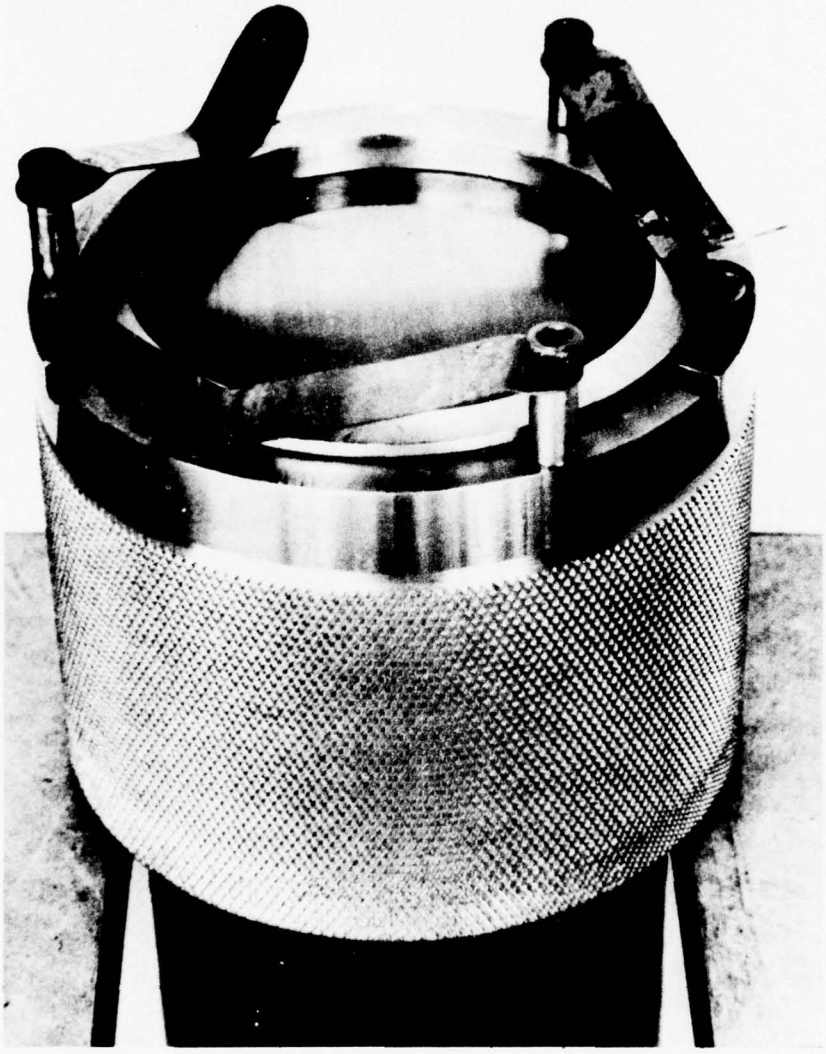

Fig. 4a. Photograph of assembly corresponding to Fig. 3.

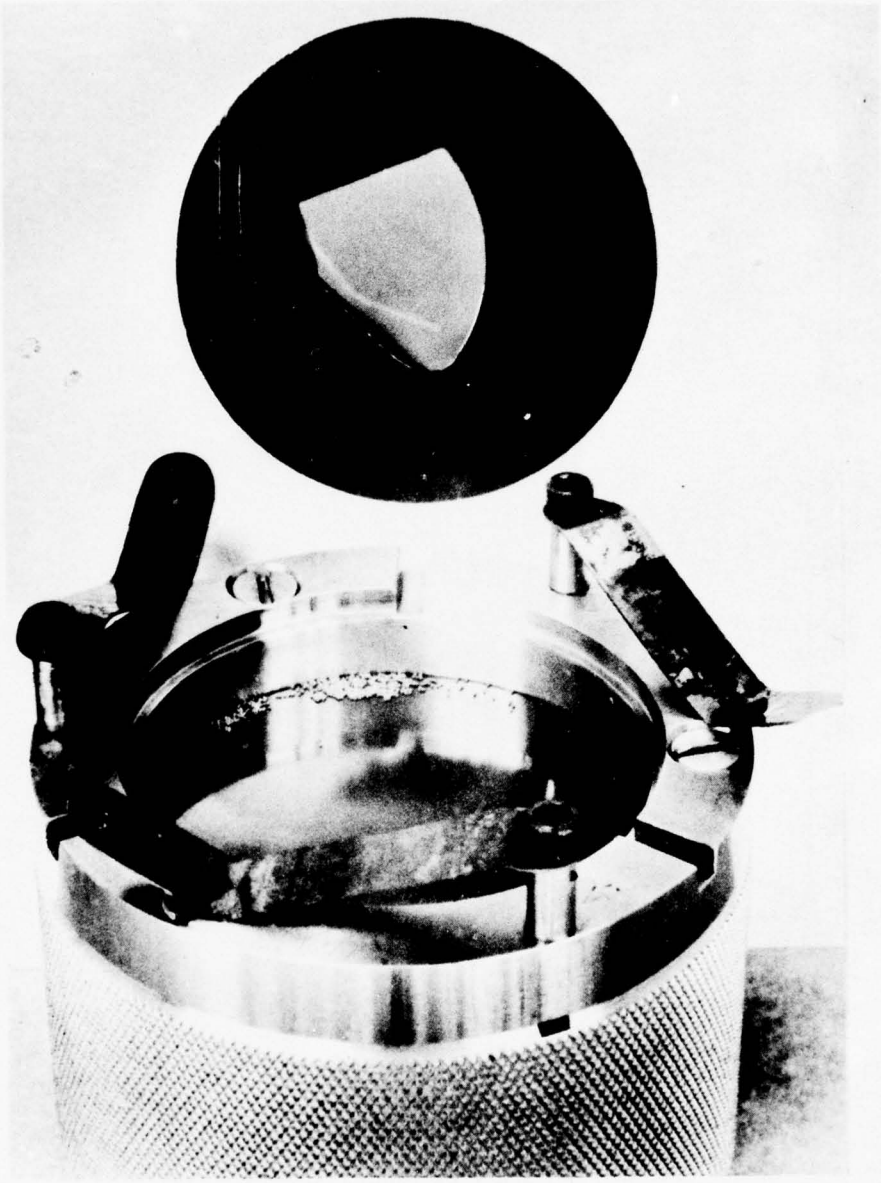

Fig. 4b. Assembly open, loaded with tungsten balls. Sample carrier membrane with sample above.

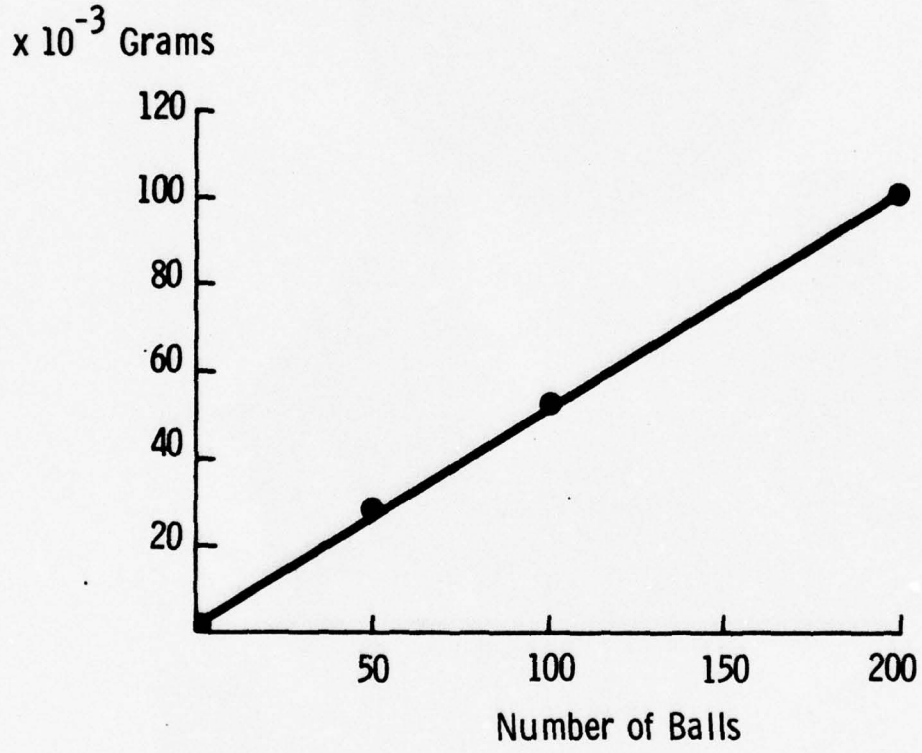

Fig. 5. Plot of weight vs. number of balls. Slope gives a value of 0.0005 g for a single ball.

The impact chamber containing the tungsten balls is formed by the two membranes and the membrane clamping ring. The driver membrane is clamped into the coupling by the membrane clamping ring, which is fastened to the coupling by three screws. In Fig. 3, the sample is shown mounted on the sample carrier membrane, which rests in the top of the membrane clamping ring. The membrane is held securely in place by the sample carrier clamping ring. This ring distributes the holding force exerted by three spring clips located 120^{o} apart around the membrane clamping ring. The spring clips may be swivelled away to facilitate removal of the sample carrier clamping ring and membrane for sample changes. Cutouts are provided in the membrane clamping ring and coupling to facilitate removal of the membranes. A knurl is provided on the outside of the coupling to facilitate installation on the sound tube, which threads into it.

The membranes are made of tempered spring steel. An analysis to determine the optimum membrane thickness is presented in the next section. The 3/8mm thickness was found to give maximum amplitude for driver input power within the specified limit, at resonant frequency. This frequency is $\approx$1000 cps when the membranes are new. However, an aging effect was noted. This results in a slight convex upward deformation of the driver membrane and an accompanying

increase of the optimum resonant frequency. Any effects of this on ISS performance can be counteracted by the monitoring system described earlier. Furthermore, other materials may be investigated for use in membranes with a view toward eliminating this aging effect.

2.2 Determination of Membrane Dimensions

A convenient membrane diameter of 5.5 cm free (unclamped) was chosen. The optimum membrane thickness was then determined by analysis.

Membrane oscillations and the occurrence of resonant modes of the driver membrane were measured using a transducer. The transducer, whose output was fed to an oscilloscope, was first placed over the impact chamber without the sample carrier membrane in place. The frequency was scanned at a driver input power (10 watts) compatible with the sensitivity of the transducer. The position and amplitude of the fundamental and harmonic modes were plotted. Results for various membrane thicknesses are given in Figs. 6-9. These results are helpful in the choice of membrane thickness.

The measurement was repeated with the sample carrier membrane, the tungsten balls, and the sample to be stressed in place. The results showed a negligible change in

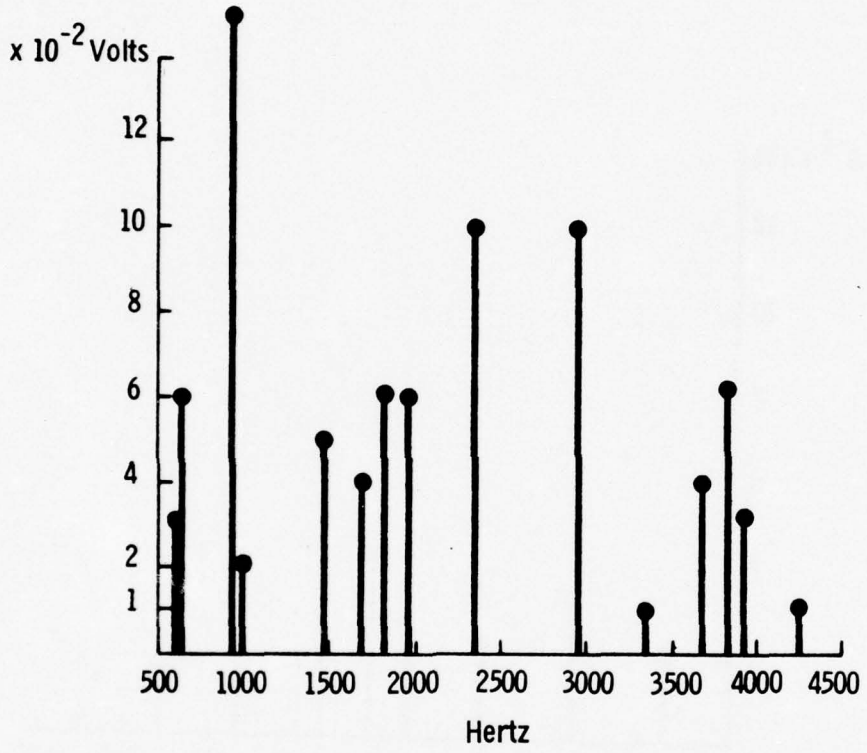

Fig. 6. Output vs. frequency of a 1/8 mm steel diaphragm.

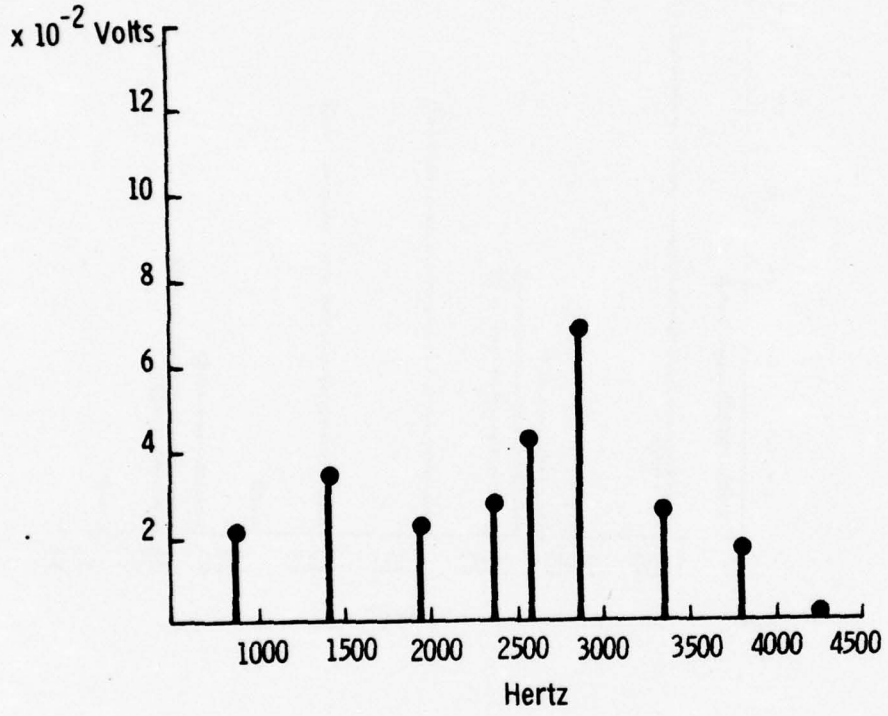

Fig. 7. Output vs. frequency of a 1/4 mm steel diaphagm.

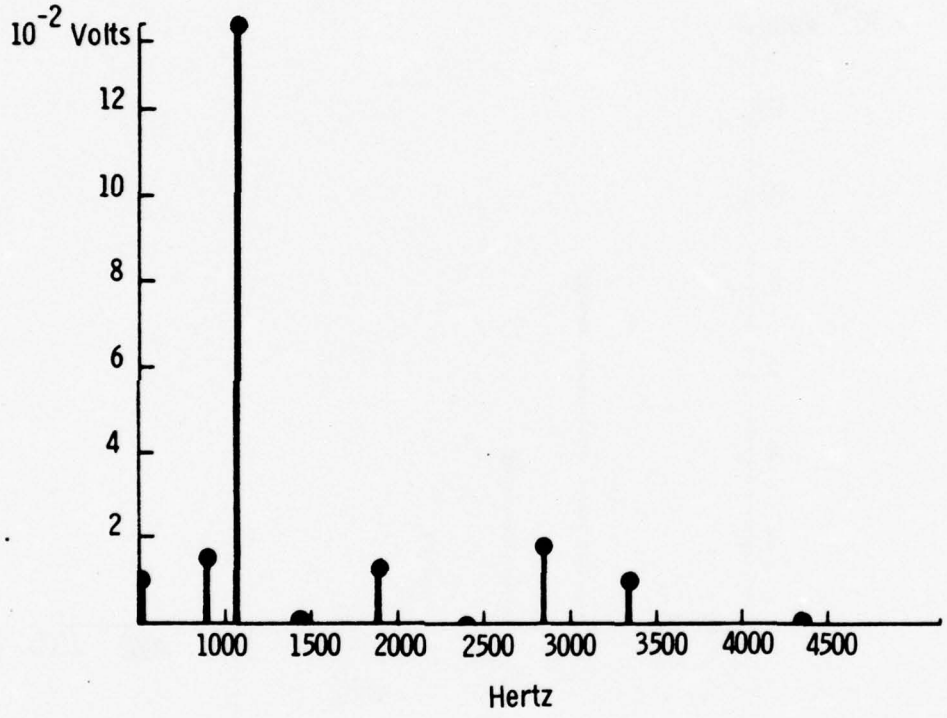

Fig. 8. Output vs. frequency of a 3/8 mm steel diaphagm.

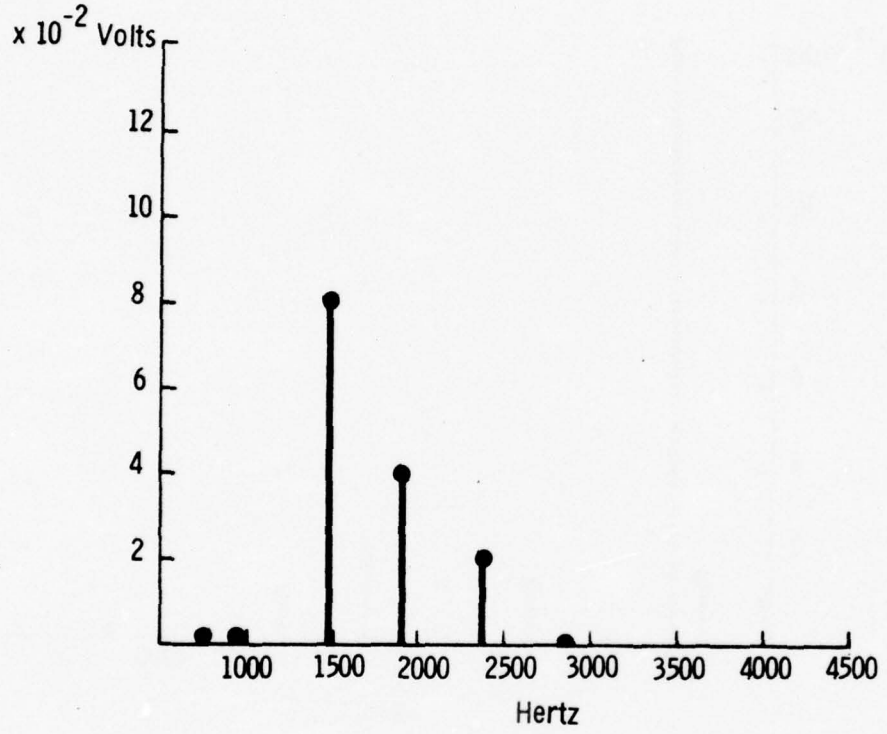

Fig. 9. Output vs. frequency of a 1/2 mm steel diaphragm.

frequency but a large change in amplitude. This indicates that, in the fully assembled configuration, the oscillations are damped but the resonance of the system is maintained.

The criterion of maximum coupling led to the selection of the 3/8mm thick membrane at a frequency of ≈ 1000 Hz.

One long term change observed was the membrane aging effect mentioned earlier. Increasing resonant frequency was coincident with a gradually increasing, permanent bowing away of the membrane from the driving force. A change of +400 Hz had occurred after about ten hours of operation. The frequency appeared to stabilize at about 1530 Hz, after continued use.

2.3 Evaluation of ISS Operational Parameters and Damage Site Density in GaAs Slices

A study of the effects of driver input power and time period of ISS application and their influence on damage site density was made. A set of curves was developed to serve as a guide for selecting optimum combinations of these operational parameters.

A group of polished samples was treated with ISS in a matrix of selected power and time settings. One thousand tungsten balls were used in the impact chamber. The samples were 1/2 mm thick, of irregular shape, and varied in surface area from 1 to 4 cm^2. Their surface orientation was (100), resistivity: 0.00349 Ω-cm, and doping: Sn - 6.5 x 10^{17}.

2.3.1 Matrix Determination

Initial experiments provided guidelines for the selection of practical values in the matrix. The experiments showed that excessive driver input power causes a catastrophic pulverization of the GaAs surface by the tungsten balls. At the lower power limit the balls fail to fracture the surface due to insufficient energy imparted to them by the driver membrane. An excessively long time period results in overlapping of damage site boundaries preventing density determination. It may also have a minor effect on surface pulverization due to increased probability of repeated impacts at the same site. Time conservation is also considered in the setting of the time period upper limit. The lower limit of time was selected to provide sufficient damage site density for microscopic studies. Sample thickness was considered, to avoid breakage at higher power levels.

The experimental matrix selected is given in Table 1:

Table 1. Experimental Matrix - Driver Input Power versus Time Period of ISS Application

Time (sec.)	Power (watts)			
	10	15	20	25
30	Run 1	Run 2	Run 3	Run 4
45	Run 5	Run 6	Run 7	Run 8
60	Run 9	Run 10	Run 11	Run 12
75	Run 13	Run 14	Run 15	Run 16

2.3.2 Damage Site Density Determination

A photomicrograph (magnification: 46X) was recorded of the ISS treated surface of each sample processed in the matrix. The number of damage sites visible within a sixteen square centimeter area on each micrograph were counted. The count was performed independently by three individuals and the three sets of statistics were averaged. The results were used to calculate the density, using the simple equation: $d = N\,(m)^2/16$; where d = density (sites/cm^2), N = number of sites per 16 cm^2 area on micrograph, and m = magnification of micrograph.

2.3.3 Matrix Data Analysis

Damage site density obtained from fourteen of the sixteen runs is plotted vs. time period in Fig. 10. Data from runs 15 and 16 was omitted since it appeared to be spurious.

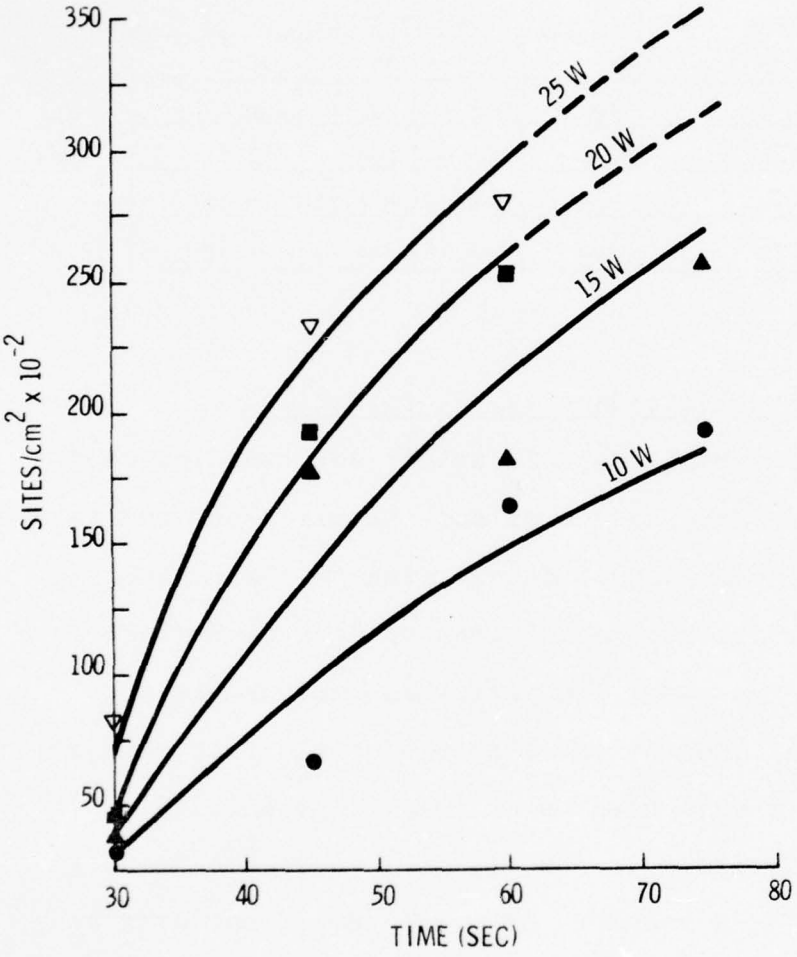

Fig. 10. ISS application time period vs. damage site density at various driver input power levels.

Constant power curves are fitted to the data points. The curves are shown terminated at the matrix time limit of 75 seconds. These curves could be extended, however, since greater densities are possible with longer time periods. Several subsequent runs made at 12.5 watts for 200 seconds yielded a density of 492 x 10^2 sites/cm^2. The non-linear shape of the curves may be due to increased overlapping of damage sites, at higher values of time and power. This would reduce the density count at those values to less than the actual impact density. The lower power curves appear to be flatter, with 10 watt curve approaching a straight line. This could be due to an effect tending to reduce densities at lower power settings, which may be explained as follows.

The tungsten balls, travelling in various trajectories within the impact chamber, produce impacts with unequal force. The proportion of impacts having insufficient energy to cause surface fracturing would therefore be higher at the lower power levels. This would then lower the damage site density for those levels.

The curves should reach a maximum when the density becomes so high that further damage sites cannot be distinguished. A theoretical value for this density limit is approximately 1670 x 10^2 sites/cm^2, neglecting overlapping effects, but assuming that the sample area is completely covered. The

value for the denstiy limit was calculated using an average area per damage site of 600 square micrometers. Distinquishable overlapping of damage sites could raise this value by a factor of three. It appears possible, however, that the balls impact the surface in certain patterns depending on the oscillating frequency. This could cause certain sample areas to remain low in damage for all practical time periods. Such an effect would set a lower countable density limit. In either case, densities approaching the limiting values may be expected to have considerable effect on the severity and variation of damage. This would be due to the high probability of repeated coincidence of ball impact sites.

In this section it is shown that while application time is the major factor influencing damage site density, driver input power also affects it. This may be due to changes in ball velocities resulting in variation of the number of impacts per unit time.

The curves in Fig. 10 indicate that both time period and input power influence the damage site density. An additional analysis of the experimental data was made to determine the relative effect of these two operating parameters.

Pairs of matrix runs made at equal power levels for different time periods were selected. The percent increase in time and the resulting increase in damage site density from the shorter to the longer run were determined. The average density increase for all pairs with the same time increase percentage, but at different power levels per pair, was calculated. This provides a measure of the influence of time alone, which is shown as curve I in Fig. 11.

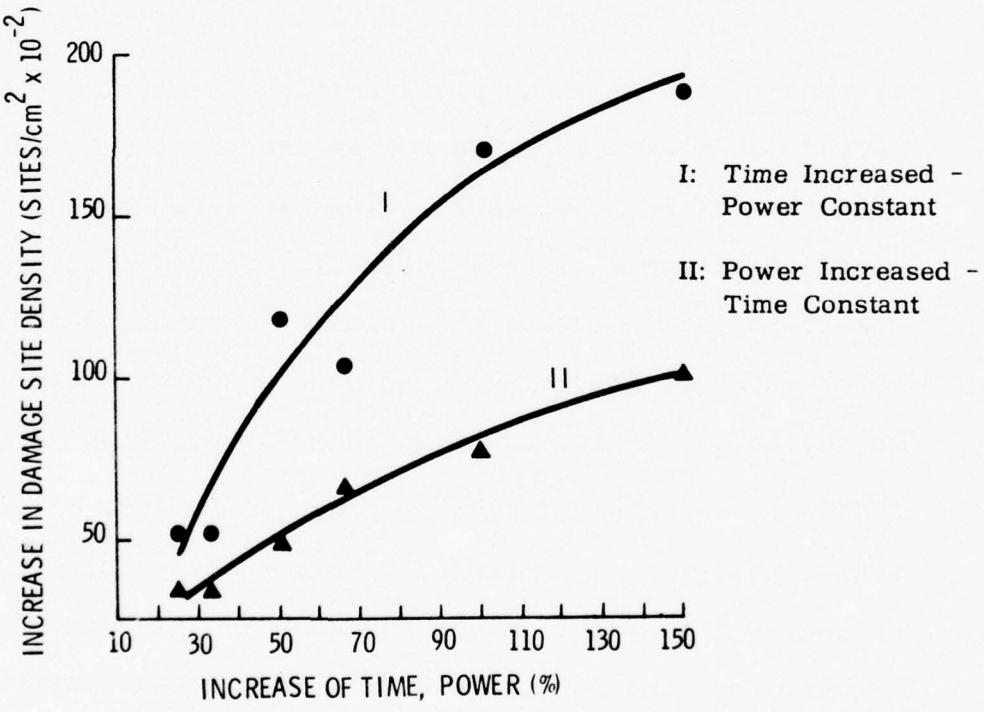

Fig. 11. Damage density vs. time dependency.

Conversely, pairs of runs made for equal time periods, at different power levels, were selected. The percent increase in power and the increase in damage site density were determined similarly. The average density increase for all pairs with the same power increase percentage, but run for different time periods per pair, gives a measure of the influence of driver input power alone. This is given with curve II in Fig. 11.

It can be seen from the plots that the length of time period has a greater influence on damage site density than has driver input power. This is shown by the location of curve I above curve II. Their positions on the graph indicate that the relative importance of time to power is about 2:1. The non-linear shape of these curves may be due to the increased probability of overlapping of impact sites when the time or power difference between the runs considered is increased. This would result in a decreased difference in density count. This effect is greater for time, as evidenced by the greater instantaneous slope of curve I, and should be in proportion to the greater influence of time on damage site density.

2.3.4 Summary for Selection of ISS Operational Parameters

The curves in Fig. 10 may be used as a guide in the selection of driver input power and time period of ISS application for given damage site densities. It must be kept in mind, however, that they may be considered valid only for the equipment and frequencies described in Sections 2.1 and 2.2, and the material described in Section 2.3. The pertinent numerical values are summarized in Table 2.

Table 2. Sample, Equipment and Operational Parameters Used for ISS Treatment of Gallium Arsenide

Parameter	Value
Sample	
Surface orientation	(100)
Thickness	1/2 mm*
Surface area	1-4 cm^2
Resistivity	0.00349 Ω-cm
Doping	Sn-6.5x10^{17}
Equipment	
Sound tube effective length	≈35cm
Sound tube inside diameter	4.7cm
Impact chamber height	8mm
Impact chamber diameter	5.5cm
Membrane free diameter	5.5cm
Membrane thickness	3/8mm
Ball diameter	≈0.3mm
Operational	
Number of balls	1000
Frequency (with new membranes)	≈1000 c/s

*Samples (1 cm x 1 cm squares) as thin as 1/4mm have been run at 12.5 watts without breakage.

Damage site density requirements depend upon the purposes for which the ISS treated material is to be used. Most requirements probably fall within the range of 15K to 30K sites/cm^2. However, as mentioned earlier, densities approaching 50K sites/cm^2 have been obtained.

Two examples are given in Fig. 12. Both samples shown were run at 12.5 watts driver input power and an oscillating frequency of 1.53 kc/sec. The sample shown in part a. was run for 50 seconds; the other one for 200 seconds. The density difference is quite apparent in these micrographs.

3. DAMAGE CHARACTERIZATION

3.1 Surface Effects

Depressions, roughly square in shape, are generated when the tungsten balls strike the GaAs surface causing the material to yield locally. The sides of the squares are aligned in [110] directions as determined by x-ray topography in conjunction with light optical microscopy. The shape of the damage sites can be seen well in Fig. 13.

The damage sites seen in the relatively low magnification micrographs of Fig. 12 have a pitted appearance. Figure 13, however, indicates a network of fine linear fractures rather

a. 50 sec; 131X magnification.

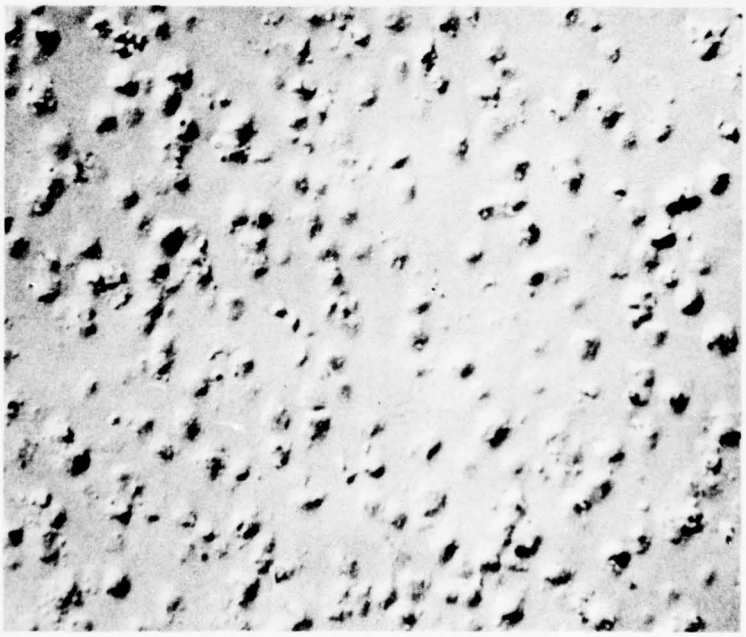

b. 200 sec; 131X magnification.

Fig. 12. ISS damage on GaAs, 12.5 watts, 1.53 kc/sec at two application time periods.

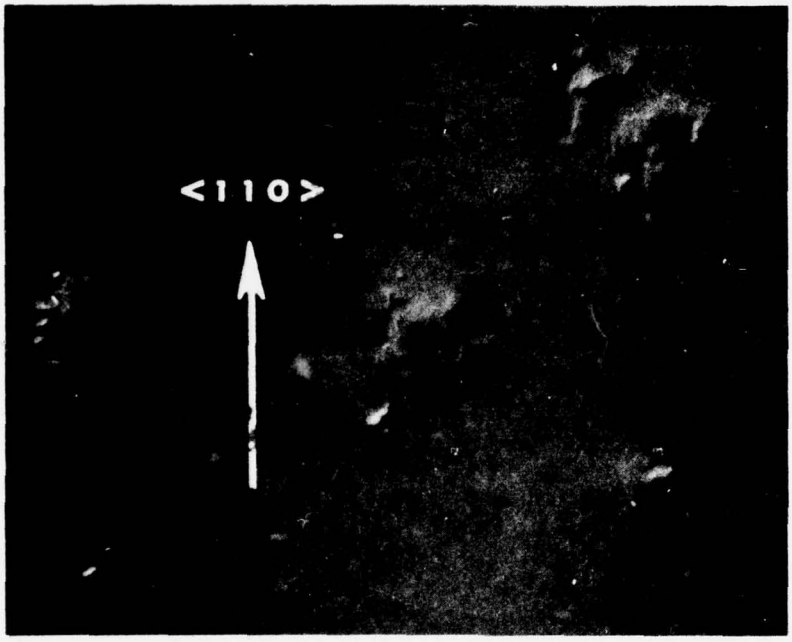

Fig. 13. Crystallographic alignment of ISS damage sites in GaAs; 855X magnification.

than pits. In the highly magnified views of Fig. 14 it becomes apparent that the damage sites consist of numerous clusters of short microcracks running normal to each other, in the same crystallographic directions as the sites themselves. The microcracks form square-shaped depressions on a smaller scale but similar to the damage sites of which they are a part.

It may not be quite clear from these light optical micrographs, taken with Nomarski contrast, whether the square-shaped areas are raised or depressed. They are, however, identified as depressions in Fig. 15. The insert in the lower left corner of the figure is a light optical micrograph (320X magnification) of a square array of ISS induced fractures in GaAs. The main portion of Fig. 15 is a scanning electron micrograph (4300X magnification) of the same array. This shows that the area between the long fractures is a depression rather than a mound as might be concluded from the insert. The SEM illustration also affords a good view of the fine linear fractures running normal to each other, especially near the lower right corner.

A long fracture with curved end can be seen at the right of the damage site in Fig. 14a. These fractures occur at some damage sites and may have either one or both ends curved. They also lie along crystallographic directions, and may be due to a stress relief mechanism.

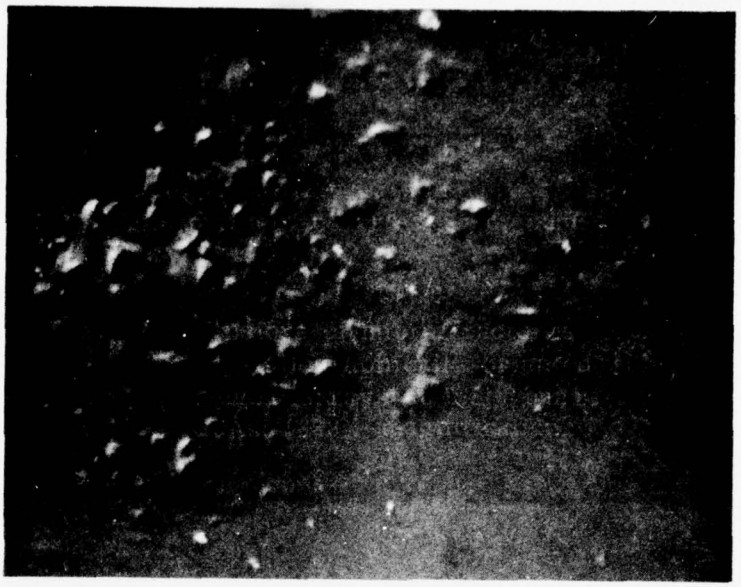

a. Note: Large fracture with curved end at right.

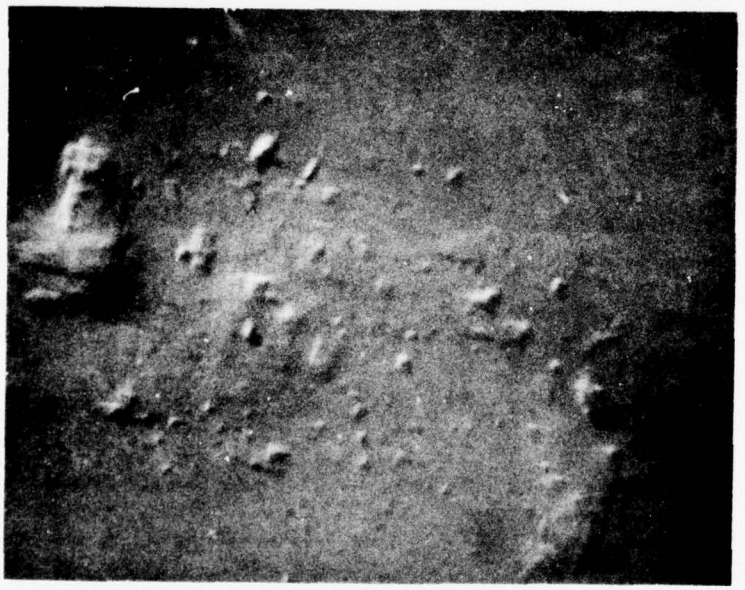

b. Note: Two larger square arrays of micro fractures at edges of damage site.

Fig. 14. Clusters of micro fractures forming crystallographically oriented [110] square arrays at ISS damage sites on GaAs; 1390X magnification.

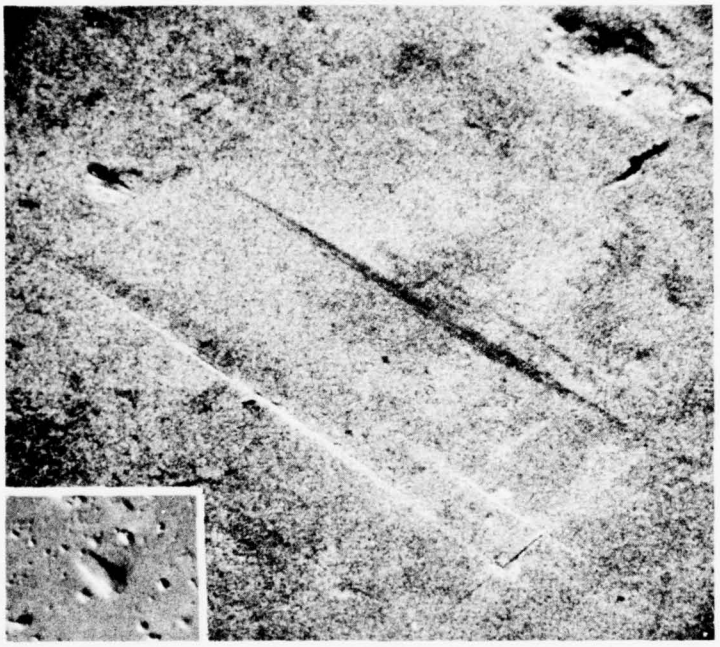

Fig. 15. Scanning electron micrograph of ISS induced square array of microcracks in GaAs; 4300X magnification. Insert shows light optical micrograph of same array; 320X magnification.

3.2 Subsurface Effects

The stresses induced by the yielding of the material at the ball impact sites produce subsurface defects such as dislocations, slip and additional micro fractures. These defects can be displayed by etching. The etching solution and technique is described in Chapter 3.

Figure 16a shows a damage site after a 15 seconds etch treatment. The insert at the bottom right corner of the micrograph shows the same site before etching at about 1/5 the magnification. Some of the original surface fractures in the foreground of the site are propagated and still visible after etching, while others have been etched away. A dense network of defects has been exposed by the etch. The two large fractures at the top and right side of the etched damage site run in crystallographic directions.

Another sample, etched for 60 seconds, is shown in Fig. 16b. This displays well the typical intricacy and profusion of the defects below the damage sites. The two fractures, indicated by arrows, lie in a crystallographic direction.

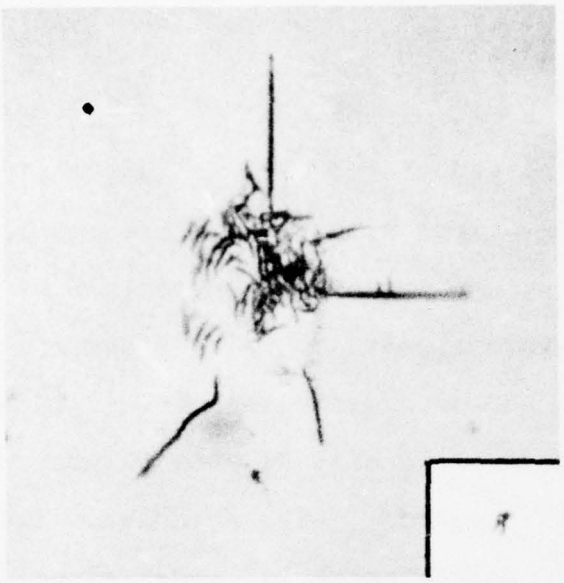

a. 15 sec etch; 855X magnification. Insert: Before etching 167X magnification.

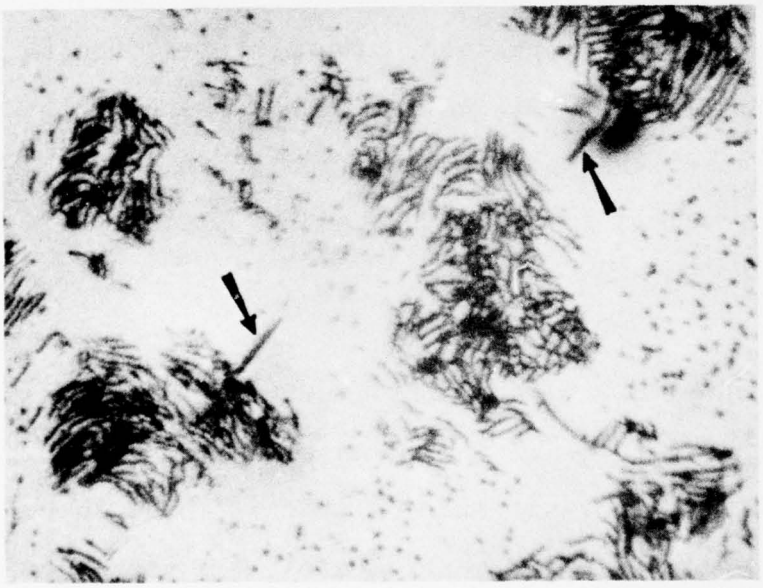

b. 60 sec etch; 855X magnification. Arrows point to fractures aligned in <110> direction.

Fig. 16. Etch figures of ISS damage sites on GaAs.

It was noted during repetitive etching that the etch figures of a given damage site first increased in size and then decreased. An example is given in Fig. 17, where the etch figure appears to reach a maximum size near steps 4 or 5 and then decreases. (This is also confirmed when the average size of etch figures at the different steps is compared.) The phenomenon indicates that the volume of defect networks generated beneath ISS damage sites is not constant for different levels into the material. Apparently it first expands to a maximum cross-sectional area and then contracts until the deepest extent of the damage is reached. The schematic sketch at the bottom of Fig. 17 illustrates this. The depth of ISS damage varies approximately from 10 to 30μm for the parameter values investigated, and is discussed in Chapter 3.

The appearance of the micrographs in Fig. 17 suggests that the etch figure is of uneven height above the general surface. This was investigated by SEM and found to be true. Apparently the damage sites etch at a slower rate than the surrounding undamaged area. This results in the etched defect grooves developing raised rims. It may

a. Before etching.

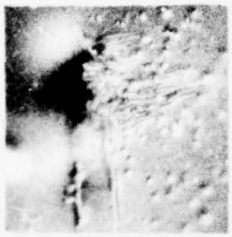

b. Step 1, 4 sec.

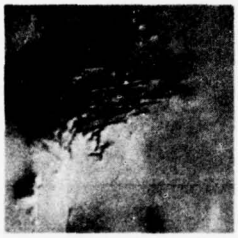

c. Step 2, 8 sec.

d. Step 3, 12 sec.

e. Step 4, 16 sec.

f. Step 5, 20 sec.

g. Step 6, 24 sec.

h. Step 7, 28 sec.

i. Step 8, 49 sec.

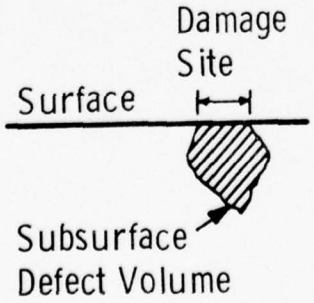

j. Schematic representation of shape of defect volume under damage site.

ISS of GaAs 69

Fig. 17. ISS damage site. Etched repetitively from 4 to 40 sec; 1130X magnification.

be noted that etch figures shown in Fig. 16 do not appear to be raised. This is an optical effect obtained by a difference in Nomarski contrast setting to accentuate the defect networks.

Detailed electron microscopy studies of ISS damage sites on GaAs surfaces are in progress but will not be completed by the end of this contract. These studies will be reported somewhere else when concluded.

4. REFERENCES

1. ARPA Report No. 4, Contract No. DAHC-72-C-0274.
2. ARPA Report No. 6, Contract No. DAHC-72-C-0274.

Chapter 3

DEPTH OF DAMAGE INDUCED IN GaAs BY IMPACT SOUND STRESSING (ISS)

by R. G. Dessauer

1. INTRODUCTION

The controlled introduction of microdamage into polished GaAs surfaces by ISS as described in Chapter 2 is useful in the study of polishing effects and fracture properties of the material.[1] It may also be employed to study effects of microdamage on device properties.[2] A knowledge of the depth of ISS microdamage is necessary for these applications.

Determination of the depth of damage is made by two separate methods, bevelling and cleaving. In the first method, samples are bevelled and subsequently etched to reveal the extent of damage down the bevel. In the latter method samples are cleaved through damaged sites and the cleavage planes are examined by scanning electron microscope.

Presently only (100) oriented samples have been examined for depth of damage.

2. EXPERIMENTAL PROCEDURES

2.1 Bevelling

2.1.1 Bevelling Procedure

The samples to be bevelled are cleaved to a convenient size along crystallographic directions as indicated by the ISS damage. They are between 400 to 500 μm thick. The cleaving procedure will be described later.

The sample is then mounted on a 2^{o} bevelling block with glycol resin. It is oriented so that the bevel lies along a crystallographic direction.

The abrasive slurry used is a suspension of 0.3 μm aluminum oxide particles in water at room temperature. The slurry is applied to a horizontal plate glass bevelling surface. The bevelling block with sample is gently placed into the slurry on the plate. Care must be taken to prevent edge chipping of the sample.

The bevel is formed by gently moving the block in the direction of the bevel edge. At the end of each stroke the block is lifted off the plate, bevel side first. Upon return to the starting position, the block is lowered gently onto the plate so that the bevelled edge makes contact last. No bevelling pressure is applied other than that provided by the 250g bevelling block. The procedure is schematically illustrated in Fig. 1.

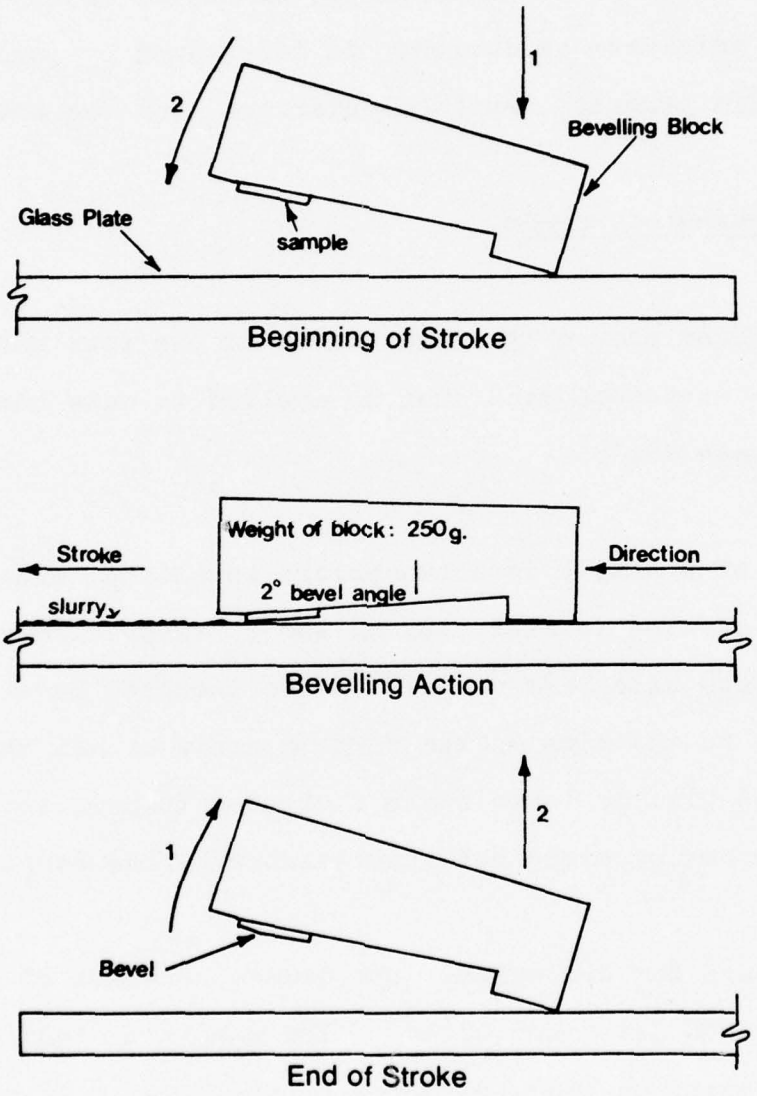

Fig. 1. Bevelling technique.

A 1.4 mm long bevel representing a depth of approximately 35 μm is sufficient for ISS damage applied with 6 to 10 watts power for about one minute. The final bevel angle, which varies due to sample thickness variations, is determined by goniometer. This permits accurate depth calculations from the bevel angle.

2.1.2 Etching of Bevels

Bevel surfaces show only a few traces of the most severe ISS damage. A structure etch must be applied to make the extent of the damage visible.

A portion of a sample is shown before bevelling, after bevelling, and after etching in Figs. 2a, b, and c, respectively. Several severe damage sites are visible on the unetched bevel in Fig. 2b. An example is the site marked with an arrow on all three micrographs. In Fig. 2c large numbers of etch figures are seen outlining the damage sites not identifiable before etching.

The etch used for delineating the damage consists of equal parts of HNO_3, HF and deionized water[3]. The sample is held with teflon coated tweezers on the side opposite the bevel. It is dipped into the etching solution bevel up. The sample is held motionless in the solution for four seconds. Three seconds are required for etching action to start as evidenced by bubbling.

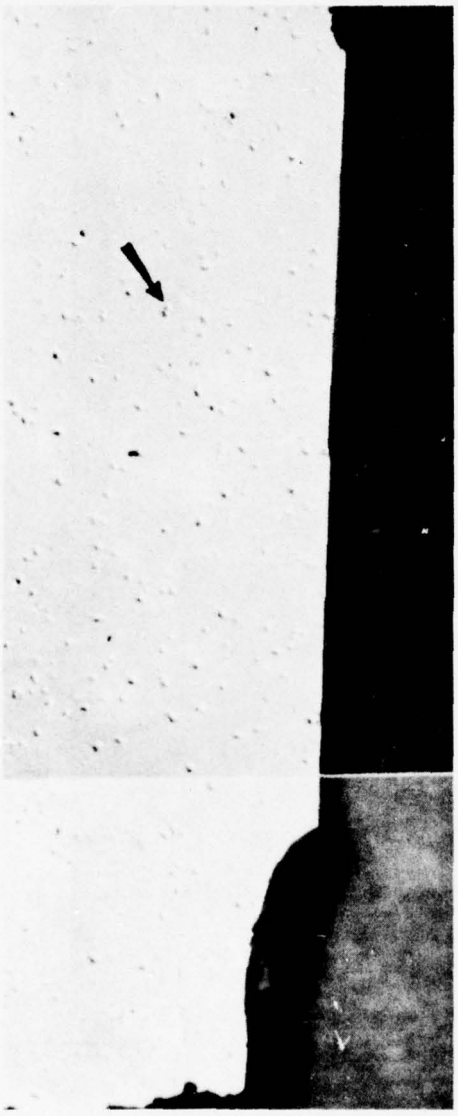

Fig. 2a. Microdamage in GaAs surface, induced by ISS at 6 1/4 watts for 60 sec. Arrow locates damage site visible in Fig. 2b. Sample ID # 6.25/1/10-21. 46X magnification.

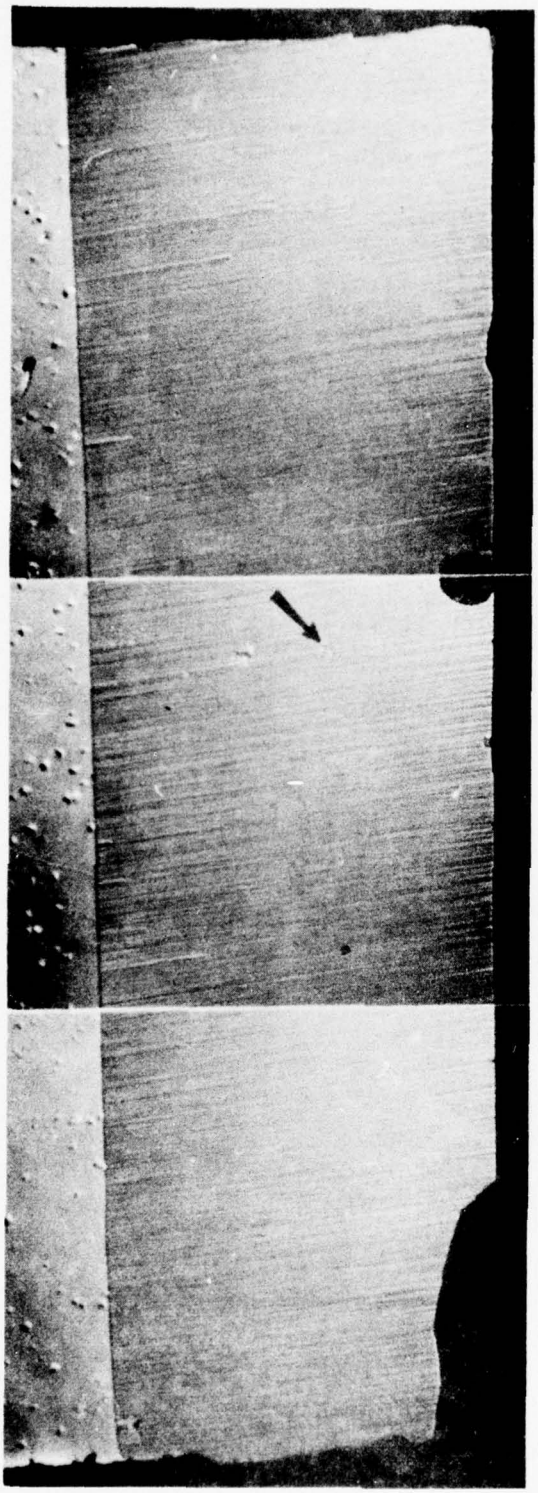

Fig. 2b. Same area as in Fig. 2a, bevelled at an angle of 1^{o} 19'. 46X magnification.

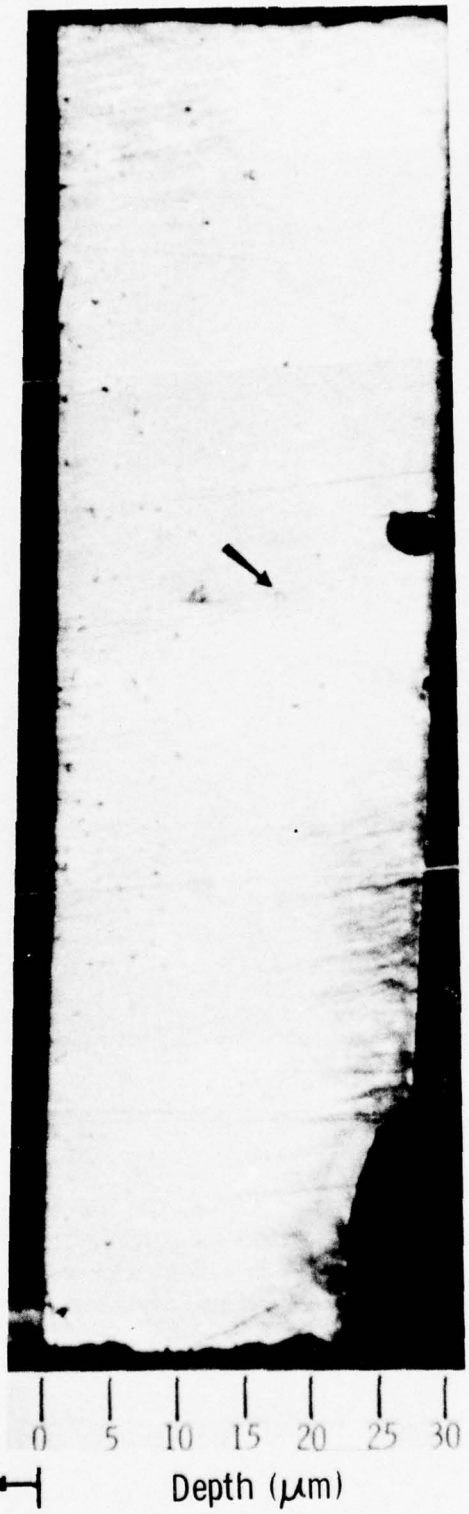

Fig. 2c. Same area as in Fig. 2b after a 4 sec structure etch; 46X magnification. Arrow locates damage site magnified in Fig. 2d.

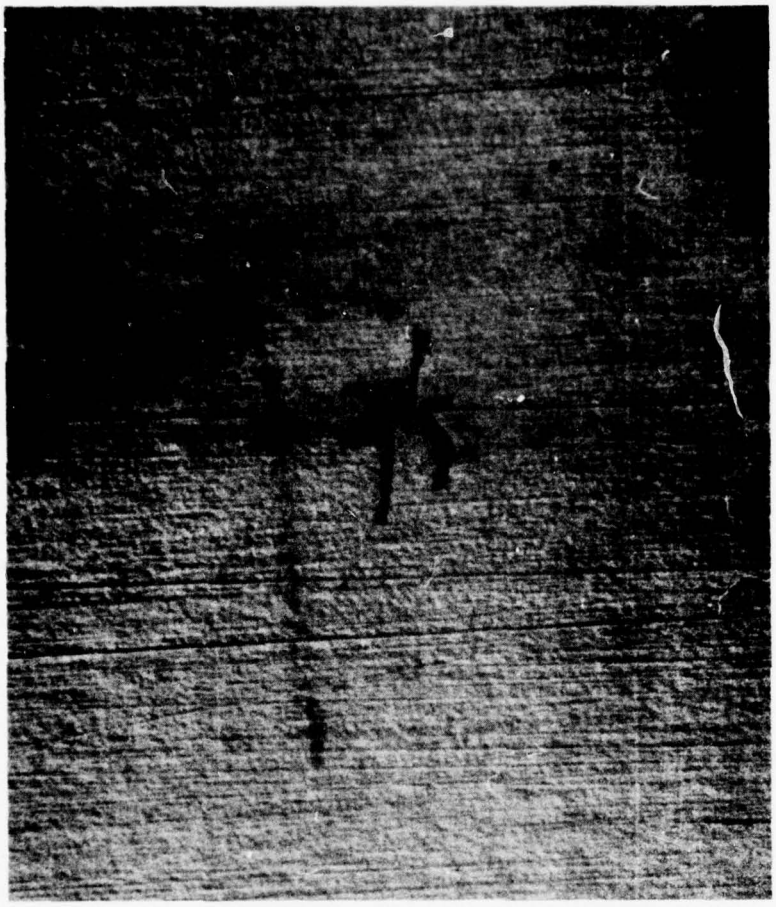

Fig. 2d. Closeup view (320X magnification) of etch figure indicated by arrow in Fig. 2c due to damage site located by arrows in Figs. 2a and 2b.

Etching time is controlled accurately with a foot switch actuated timer. The timer is started the instant the sample is dipped. It signals the end of the etching cycle with an audible signal. The sample is then withdrawn and immediately quenched in water.

2.1.3 Identification of Etched ISS Damage on Bevels

A band of damage delineated by the etching extends down from the intersection of the bevel with the sample surface (Fig. 2c).

In addition, scattered etch figures are seen farther down the bevel. Some of these may be due to other causes such as contamination, imbedded abrasive particles, or extraneous surface damage. Determination of the maximum depth of damage necessitates identification of these figures as ISS damage. This is accomplished by either one or both of two procedures. The questionable etch figures are first examined for typical appearance by high magnification light optical microscopy and scanning electron microscopy. Additional identification may be made, if necessary, by location correlation with micrographs of the area in question *taken before bevelling.* The closeup view of the etch figure shown in Fig. 2d reveals that it has the "typical" appearance. It can also be correlated with a damage site in Fig. 2a. Its location, 115 mm from end of bevel and 23 mm from edge of bevel measured on micrograph 2c, corresponds to that of a heavy damage site at a location measured similarly on micrograph 2a. The etch figure is thus identified as outlining ISS induced damage.

Some examples of etch figures typical for ISS damage are compared with etch figures due to extraneous causes in Fig. 3. Two low magnification (46X) micrographs showing sections of an etched bevel are given in Fig. 3a. The etch figures being compared are indicated by numbered arrows. They are shown magnified in detail in Fig. 3b. Etch figures 1, 3, and 7 (Figs. 3b-1, 3b-3, and 3b-7) are not due to ISS induced damage. The remaining four etch figures are typical of etched ISS induced damage and are thus identified. The long etched out grooves are due to fractures and the short feathery ones are etched dislocation chains. Figs. 3b-2, 3b-4, and 3b-6 are good examples. The two lower micrographs in Fig. 3b-4 are SEM recordings. The lowest one gives a closeup view clearly showing the etched grooves. The lower micrograph in Fig. 3b-6 gives another such example. The upper edges of the fractures seen in the SEM micrograph of Fig. 3b-5 appear broken away. This may have occurred during bevelling.

Etch figure 1, at high magnification, is seen to be a shallow surface disturbance atypical of ISS damage. Etch figure 3 is identified in the SEM micrograph as a form protruding from the surface. It may be an imbedded aluminum oxide particle carried to its site in the abrasive slurry during bevelling. The SEM micrograph in the lower portion of Fig. 3b-7 shows that etch figure 7 has none of the typical etched grooves of ISS damage. It may be due to surface contamination.

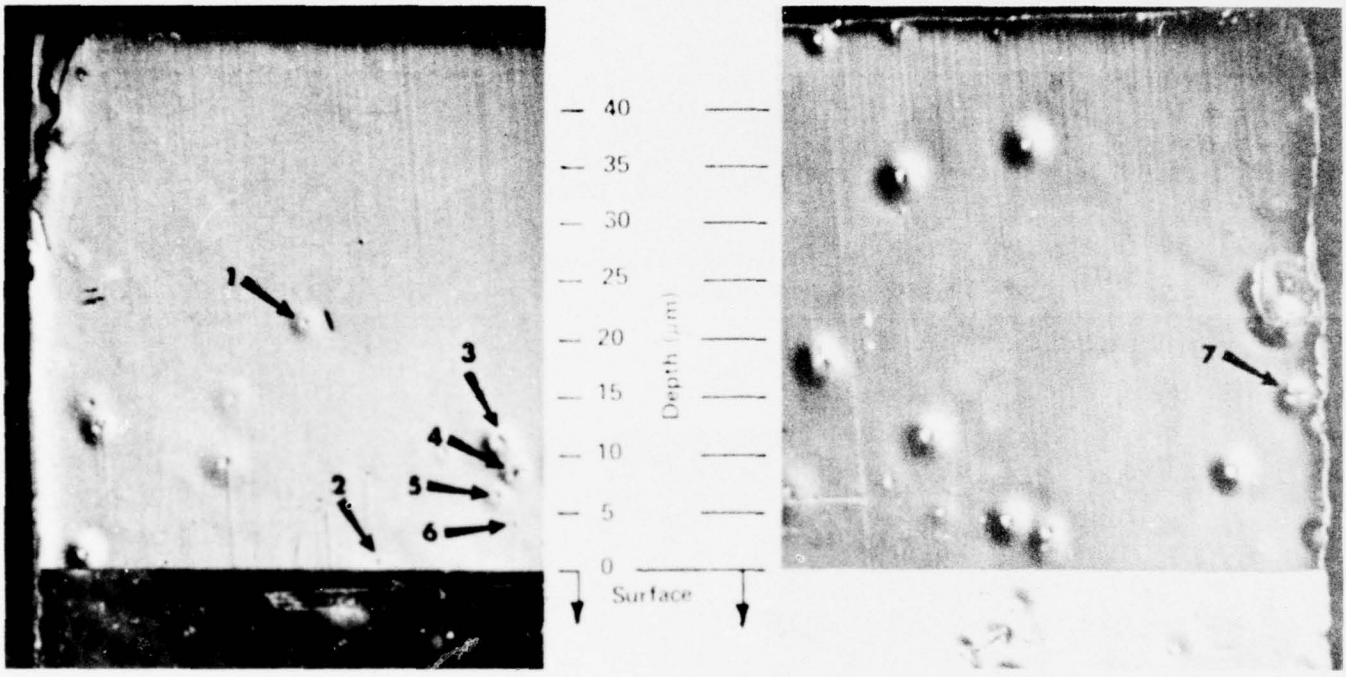

Fig. 3a. Sections of etched bevel on ISS damaged GaAs. Bevel angle is 1^{O} 32', sample ID #6.25/a/10-21; 46X magnification. Numbered arrows mark etch figures magnified in Figs. 3b-1 through 3b-7.

Fig. 3b-1. Etch figure not due to ISS damage; 855X magnification.

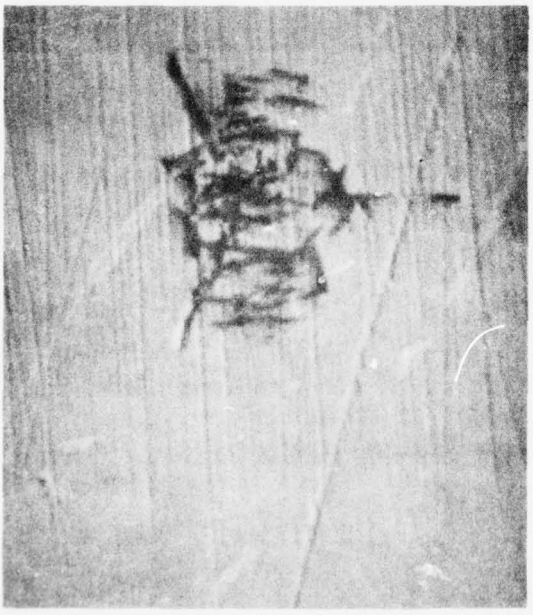

Fig. 3b-2. Etch figure due to ISS damage; 1390X magnification.

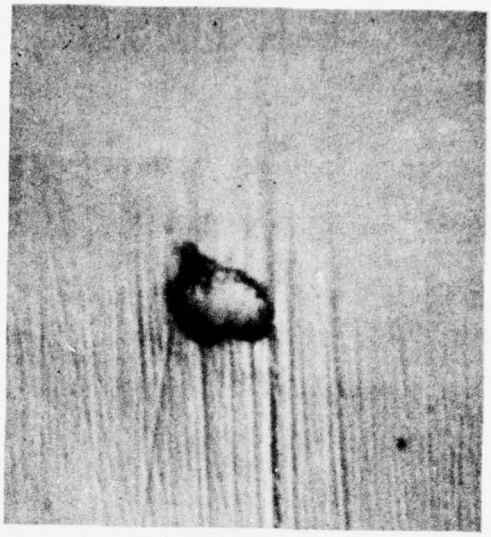

Light optical micrograph; 1390X magnification.

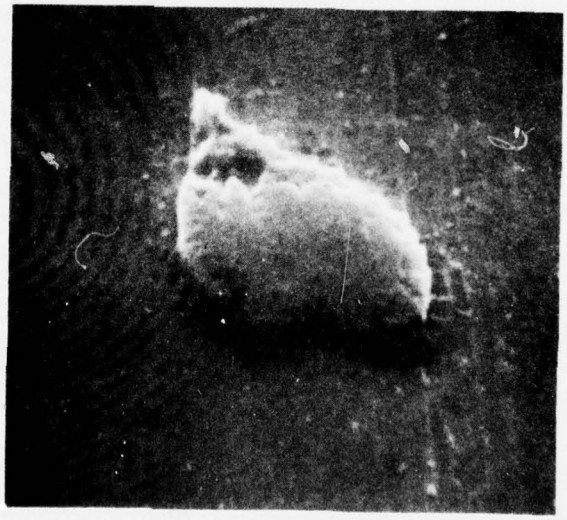

SEM micrograph; 4.7 KX magnification.

Fig. 3b-3. Particle on etched bevel.

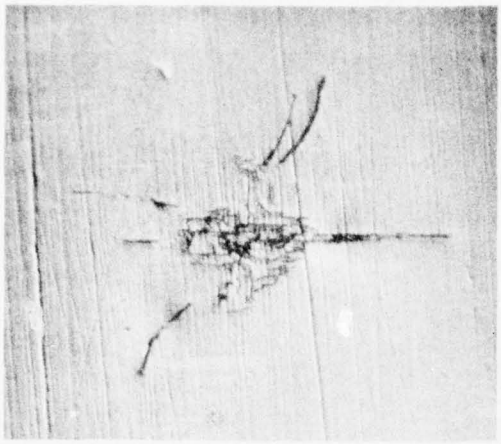

Light optical micrograph;
900X magnification.

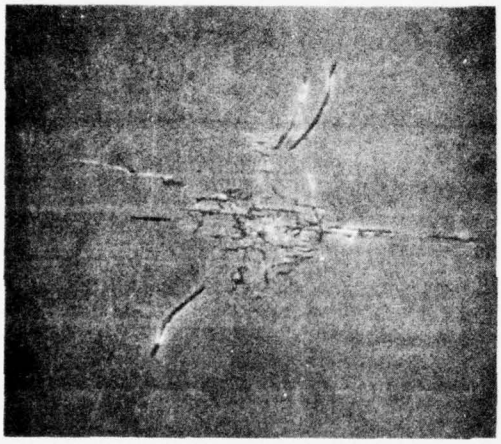

SEM micrograph; 940X magnification.

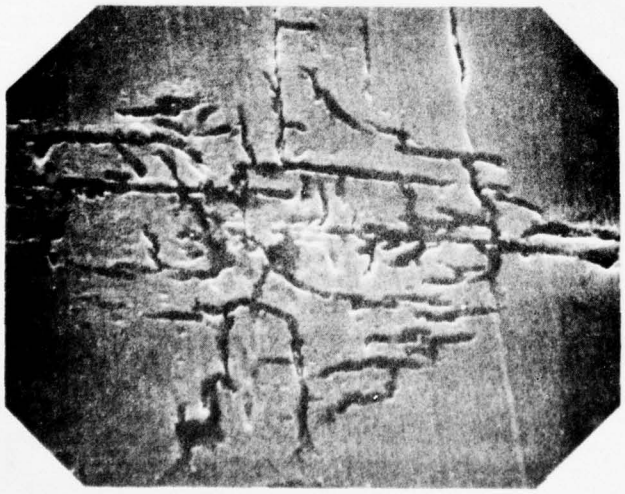

Central view of etch figure
shown above;
3.2KX magnification.

Fig. 3b-4. Etch figure due to ISS damage.

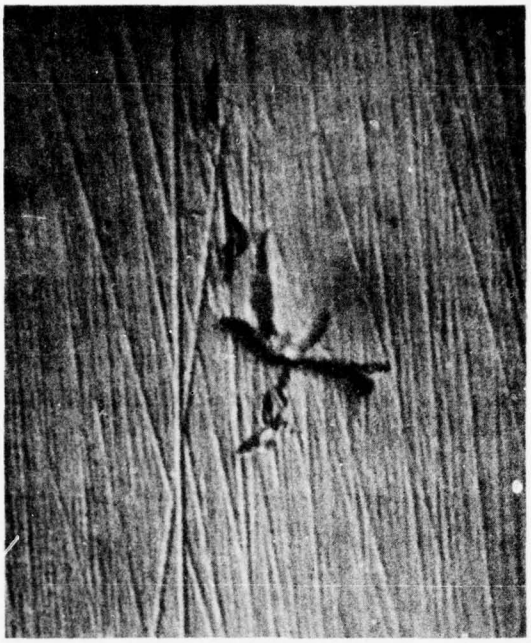

Light optical micrograph; 1390X magnification.

SEM micrograph showing broken edges on some grooves; 4.7KX magnification.

Fig. 3b-5. Etch figure due to ISS damage.

Light optical micrograph; 900X magnification.

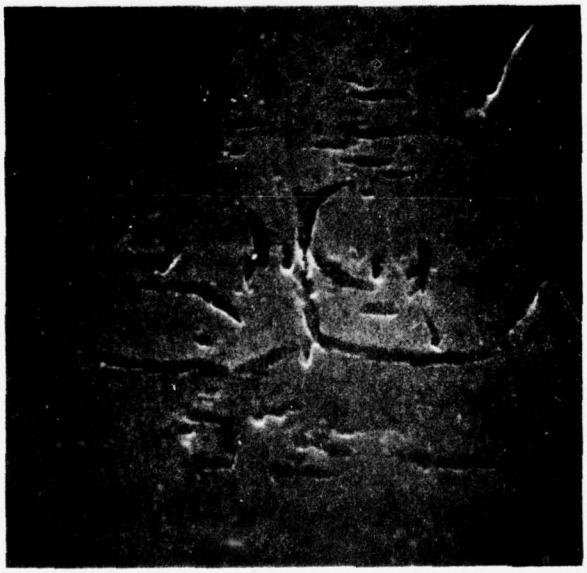

SEM micrograph; 3.2 KX magnification.

Fig. 3b-6. Etch figure typical of ISS damage.

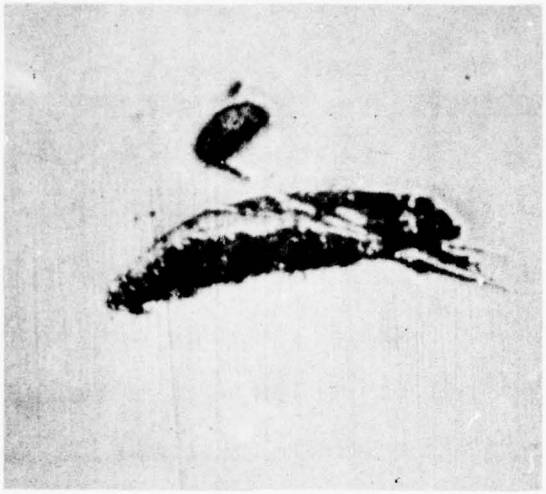

Light optical micrograph; 855X magnification.

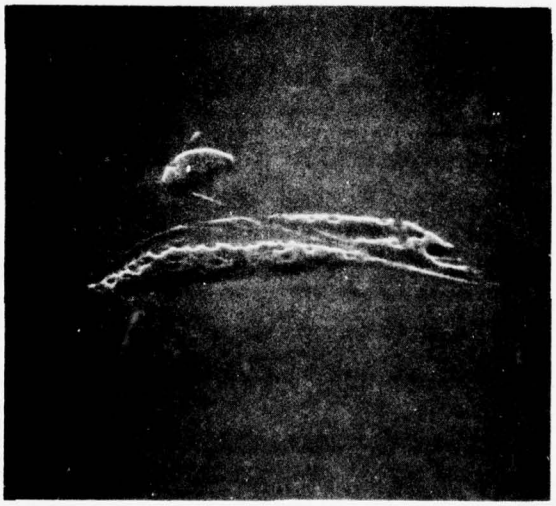

SEM micrograph; 900X magnification.

Fig. 3b-7. Etch figure not due to ISS damage. Possibly caused by surface contamination.

2.2 Cleaving

2.2.1 Cleaving Procedure

The samples to be cleaved are placed on a sheet of filter paper with the polished side containing the damage facing down. The paper forms a resilient base. The edge of a glass slide is placed along the desired crystallographic direction and a slight pressure exerted until the sample cleaves. A clean and accurate cleavage plane is obtained by this method.

2.2.2 Identification of Damage Sites on Cleavage Plane

Damage sites on cleavage planes must be properly identified. This is to avoid errors which would occur if extraneous chipping and other non-ISS induced damage were included in depth of damage measurements.

The area on the sample surface adjacent to the cleavage plane to be examined is photographed by light optical microscopy at low magnification (46X). In observing the fine surface fractures at the damage sites, considerably better contrast (and at lower magnification) is obtainable with light optical than with scanning electron microscopy.

These surface micrographs include the end of the sample or other identifying marks in addition to any damage sites which have been cleaved through. Similar micrographs are then taken of the cleavage

plane. The two groups of micrographs or montages are aligned by the noted identifying marks. Damage sites may then be located on the cleavage plane visually or, if necessary, by linear measurements taken from the end of the sample, or from other identifying marks.

Damage depth measurements can be made on light optical micrographs of the cleavage plane at up to about 200X magnification. Considerably better accuracy is obtained with the scanning electron microscope where magnifications of more than a factor of ten higher is obtainable due to its great depth of field.

The light optical micrographs are used as a guide to locate the damage sites on the cleavage plane in the SEM at a similar magnification. The cleavage passing through an ISS damage site causes part of the fractured volume to collapse and fall out. This provides excellent contrast in the SEM and the sites are easily located for subsequent high magnification recording. The procedure is illustrated in Fig. 4.

Figure 4a shows the surface of a cleaved sample in the top micrograph. The arrow points to a damage site which has been cleaved through. An edge view of the same area is given below the surface micrograph, with the damage site identified on the cleavage plane. Magnified views of the area of the damage site are given in Fig. 4b.

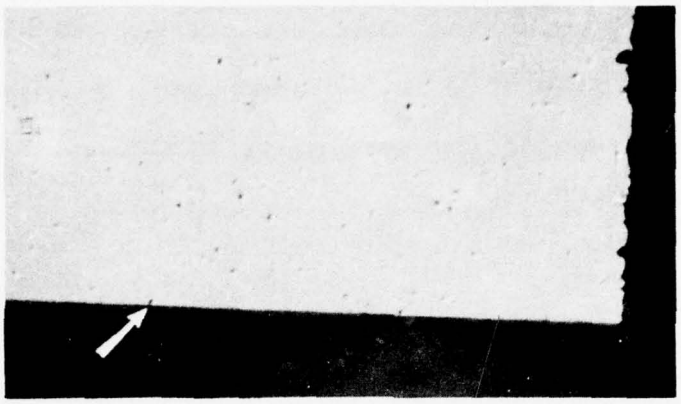

Surface; 46X magnification.

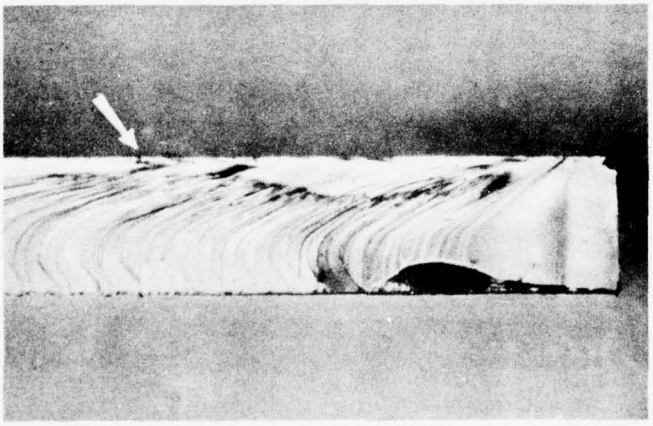

Cleavage plane; 46X magnification.

Fig. 4a. Cleaved, ISS damaged GaAs sample, sample ID # 6.25/1/10-21. Arrows indicate cleaved through damage site.

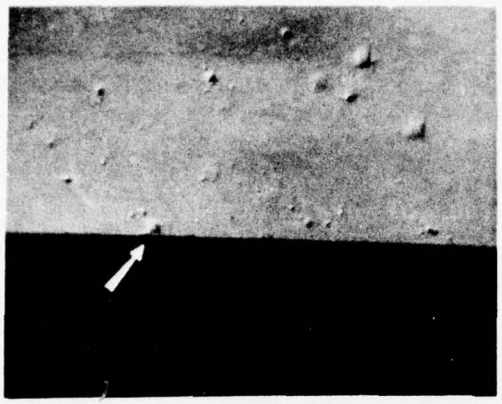

Light optical micrograph of surface;
167X magnification.

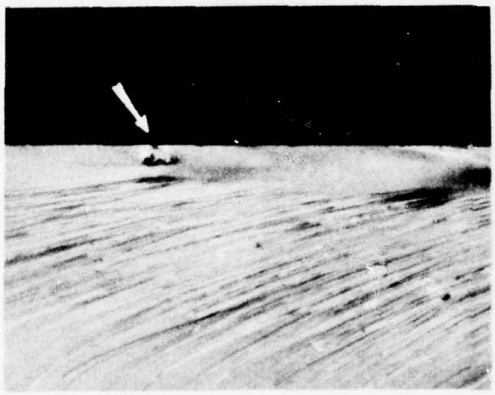

Light optical micrograph of cleavage plane;
167X magnification.

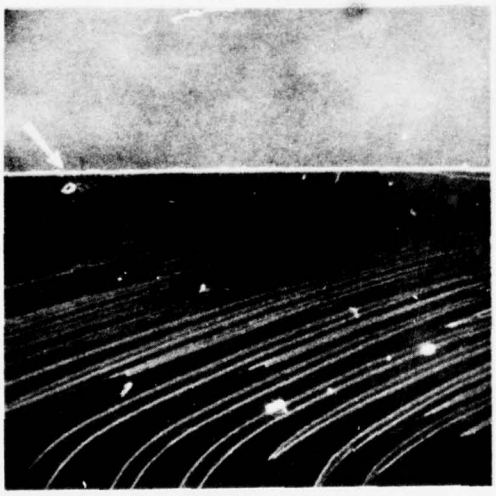

SEM micrograph of cleavage plane;
200X magnification.

Fig. 4b. Magnified view of damage site shown in Fig. 4a for location in SEM.

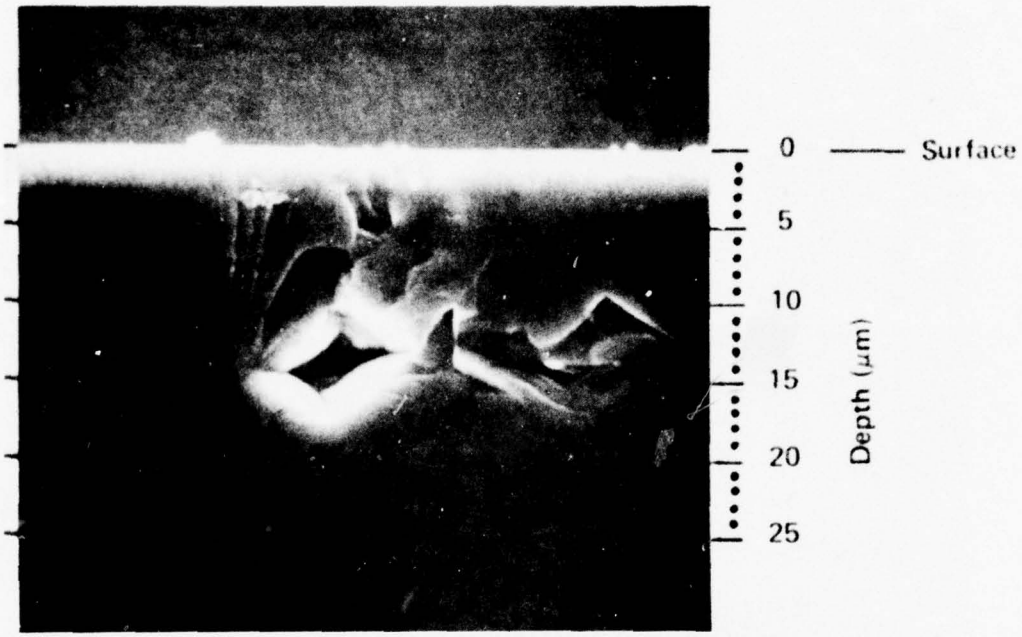

Fig. 4c. High magnification SEM micrograph of damage site on cleavage plane located in Fig. 4b; 2KX magnification. Depth of damage scales 17.75μm.

The edge view at the center is used as a guide to locate the damage site in the scanning electron microscope. A slightly more magnified scanning electron micrograph of the same area is given below. This shows where the damage site has been identified on the cleavage plane. Figure 4c shows the final scanning electron micrograph of the damage site on the cleavage plane taken at 2000X magnification. The cleavage plane is placed perpendicular to the electron beam for recording. This avoids foreshortening and allows direct depth measurements from the micrograph.

3. RESULTS

The samples examined give an indication as to the depth of damage to be expected from 60 sec ISS runs at 6 1/4 to 10 watts power. The bevels showed a high damage density band reaching to a depth of about 10 μm. Maximum depth for individual damage sites ranged to over 27 μm. Table 1 below gives the details for four bevels. The first number of the sample identification represents the driver input power in watts used for each run.

Table 1. Depth of ISS Damage in GaAs as Measured on Bevels

Sample Identification	Bevel Angle	Maximum Damage Depth (μm)	Resistivity
6.25/a/10-21	1° 32'	14.5	(>10 Ω-cm)
6.25/c/10-21	1° 34'	19.0	(>10 Ω-cm)
6.25/1/10-21	1° 19'	19.2	(>10 Ω-cm)
10/10-22	1° 16'	27.4	(≈0.001Ω-cm)

Maximum depth measurements on bevels are made in the standard manner. The perpendicular distance from the bevel/surface intersect to the farthest delineated damage site on the bevel is measured directly on the micrograph. The following equation is then applied.

$$d = \frac{10^3}{m} (L \tan \alpha)$$

where d = depth of damage in microns

L = distance measured on micrograph in millimeters

α = bevel angle (measured on goniometer)

m = magnification of micrograph

The maximum damage depth found by cleaving correlates well with that determined by the bevelling technique.

The damage sites cleaved through are located on the cleavage plane and are micrographed by SEM at 2000X magnification or higher. The depth is calculated from measurements made directly on the micrograph and the magnification.

Maximum depth of damage approaches 26 μm, which is in the same order of magnitude found with bevelling. Table 2 gives depths found on six cleavage planes. Driver input power is shown in Table 1.

TABLE 2. Depth of ISS Damage in GaAs as Measured on Cleavage Planes

Sample Identification	Maximum Damage Depth (μm)	Resistivity	Number of Sites Measured	Average Damage Depth (μm)
10/9-29	13.6	>10 Ω-cm	-	-
6.25/1/10-21 (plane a.)	17.8	>10 Ω-cm	-	-
10/10-22 (plane a.)	23.5	≈ 0.001 Ω-cm	-	-
6.25/1/10-21 (plane b.)	25.8	>10 Ω-cm	8	19.3
10/10-22 (plane b.)	24.8	≈ 0.001 Ω-cm	27	16.5
10/LD-784	15.3	0.00349 Ω-cm	6	12.7

Damage on any given sample reaches a range of varying depths at different sites. This is due to the tungsten balls, in various trajectories, impacting with unequal force and impact angle.

4. CONCLUSION

ISS damage induced at 10 watts power, for 60 seconds, reaches a maximum depth approaching 30 μm. Most of the damage sites reach a depth of 10 μm. A decreasing number reaches deeper than 10 μm, and a small percentage reaches maximum depth of ≈30 μm.

Resistivity does not appear to be a depth determining factor.

It might be expected that depth would vary somewhat with power settings and, due to repeated impacts, even with time. Tests

AD-A032 697 INTERNATIONAL BUSINESS MACHINES CORP HOPEWELL JUNCTIO--ETC F/G 20/2
DEFECT STRUCTURE IN GAAS.(U)
SEP 76 G H SCHWUTTKE F19628-75-C-0174
UNCLASSIFIED IBM-TR-22.2065 RADC-TR-76-256 NL

2 OF 2
ADA032697

END

DATE
FILMED
2 - 77

indicate, however, that this may not be very significant within the limits of the experimental matrix described in Chapter 2.

Two effective methods for determining ISS damage depth in GaAs have been developed. The methods, bevelling and cleaving, are complementary. Cleaving is more convenient, but good accuracy requires use of a scanning electron microscope.

5. ACKNOWLEDGEMENT

The bevelling technique was developed and all bevelling was done by Mr. Edward F. Gorey.

6. REFERENCES

1. ARPA Report No. 4, Contract No. DAHC 15-72-C-0274.
2. ARPA Report No. 6, Contract No. DAHC 15-72-C-0274.
3. A. F. Bogenschuetz, "Etching of Semiconductors," published by Carl Hanser Verlag, Munich 1967.

MISSION
of
Rome Air Development Center

RADC plans and conducts research, exploratory and advanced development programs in command, control, and communications (C^3) activities, and in the C^3 areas of information sciences and intelligence. The principal technical mission areas are communications, electromagnetic guidance and control, surveillance of ground and aerospace objects, intelligence data collection and handling, information system technology, ionospheric propagation, solid state sciences, microwave physics and electronic reliability, maintainability and compatibility.

Printed by
United States Air Force
Hanscom AFB, Mass. 01731